Inhibitory G proteins play multiple roles to polarize sensory hair cell morphogenesis

Amandine Jarysta[1], Abigail L.D. Tadenev[1], Matthew Day[1], Barry Krawchuk[1], Benjamin E. Low[1], Michael V. Wiles[1], and Basile Tarchini[1,2 #]

[1]The Jackson Laboratory, Bar Harbor, ME 04609, USA. [2]Tufts University School of Medicine, Boston, MA 02111, USA.

[#]Corresponding author: basile.tarchini@jax.org

ABSTRACT

Inhibitory G alpha (GNAI or Gαi) proteins are critical for the polarized morphogenesis of sensory hair cells and for hearing. The extent and nature of their actual contributions remains unclear, however, as previous studies did not investigate all GNAI proteins and included non-physiological approaches. Pertussis toxin can downregulate functionally redundant GNAI1, GNAI2, GNAI3 and GNAO proteins, but may also induce unrelated defects. Here we directly and systematically determined the role(s) of each individual GNAI protein in mouse auditory hair cells. GNAI2 and GNAI3 are similarly polarized at the hair cell apex with their binding partner GPSM2, whereas GNAI1 and GNAO are neither detected nor polarized. In *Gnai3* mutants, GNAI2 progressively fails to fully occupy the subcellular compartments where GNAI3 is missing. In contrast, GNAI3 can fully compensate for the loss of GNAI2 and is essential for hair bundle morphogenesis and auditory function. Simultaneous inactivation of *Gnai2* and *Gnai3* recapitulates for the first time two distinct types of defects only observed so far with pertussis toxin: 1) a delay or failure of the basal body to migrate off-center in prospective hair cells, and 2) a reversal in the orientation of some hair cell types. We conclude that GNAI proteins are critical for hair cells to break planar symmetry and to orient properly before GNAI2/3 regulate hair bundle morphogenesis with GPSM2.

INTRODUCTION

Developing sensory hair cells (HCs) in the inner ear undergo a complex polarization process to detect and interpret mechanical stimuli, including sound. Each mature HC is able to detect stimuli in a directional manner by developing an asymmetric brush of actin-based membrane protrusions, or stereocilia: the hair bundle. Neighboring HCs also adopt concerted orientations to align their hair bundles, a property known as planar cell polarity (PCP). One subclass of heterotrimeric guanine nucleotide-binding (G) protein was intimately associated with different levels of mouse HC polarization: inhibitory G alpha subunits (GNAI1, GNAI2, GNAI3 and GNAO; collectively GNAI or Gαi). However, several roles proposed for GNAI proteins have not been validated physiologically, and the individual contribution of each GNAI remains uncertain.

HC polarization along the epithelial plane starts with the off-center migration of the basal body and its associated primary cilium, the kinocilium (Denman-Johnson & Forge, 1999; Mbiene & Sans, 1986; Tilney et al, 1992). At that stage, Regulator of G protein Signaling 12 (RGS12) is required for GNAI and the G protein signaling modulator 2 (GPSM2) scaffold to form a polarized complex at the apical membrane on the side of the off-center basal body (Akturk et al, 2022; Ezan et al, 2013; Tarchini et al, 2013). GPSM2-GNAI is best known as a highly conserved protein complex orienting the mitotic spindle during progenitor divisions (Du et al, 2001; Schaefer et al, 2001; Schaefer et al, 2000; Woodard et al, 2010). In post-mitotic HCs, GPSM2-GNAI first excludes microvilli and microvilli-derived stereocilia from the portion of the HC surface where it resides, the expanding bare zone (Figure 1A). Bare zone expansion then pushes back the basal body/kinocilium from a more eccentric position near the lateral junction to a less eccentric position at the vertex of the forming hair bundle. Later, GPSM2-GNAI becomes enriched at the distal tip of row 1 stereocilia abutting the bare zone (Tarchini et al, 2016). In these stereocilia, GPSM2-GNAI is a module of the elongation complex that also comprises MYO15A, WHRN and EPS8 (Mauriac et al, 2017; Tadenev et al, 2019). GPSM2-GNAI is required at row 1 tips for boosting enrichment of other elongation complex partners, and presumably actin incorporation, compared to further

stereocilia rows. GPSM2-GNAI thus confers row 1 its tallest identity and the hair bundle its asymmetric graded-height morphology.

Pertussis toxin (ptx) has been extensively used as a tool to ADP-ribosylate the GNAI subunit and dissociate heterotrimeric G protein complexes from GPCRs to inactivate downstream signaling (Locht et al, 2011). *In vivo* expression of ptx catalytic subunit (ptxA) prevents normal enrichment and polarization of GPSM2-GNAI in developing HCs (Tadenev et al, 2019; Tarchini et al, 2013), suggesting that ADP-ribosylation directly or indirectly inhibits GPSM2-GNAI function as well. Ptx recapitulates severe stereocilia stunting and immature-looking hair bundles observed when GPSM2 or both GNAI2 and GNAI3 are inactivated (Beer-Hammer et al, 2018; Mauriac et al, 2017; Tadenev et al, 2019; Tarchini et al, 2016). In contrast, stereocilia height is more variably reduced in *Gnai3* single mutants, with defects more severe at the cochlear base (Beer-Hammer et al, 2018; Mauriac et al, 2017). This can explain why hearing loss is more severe at high frequencies in *Gnai3* mutants, but profound at all frequencies in a *ptxA* model and in mutants lacking GPSM2 or both GNAI2 and GNAI3 (Beer-Hammer et al, 2018; Mauriac et al, 2017; Tarchini et al, 2016). Surprisingly, before affecting hair bundle differentiation at postnatal stages, ptx also causes two distinct defects in HC polarization at embryonic stages.

First, one study reported that a high dose of ptx in cultured explants of the developing cochlea resulted in a low proportion of symmetrical HCs with a central kinocilium surrounded by a rounded hair bundle (Figure 1B) (Ezan et al, 2013). Because GPSM2-GNAI recruits partners to pull on astral microtubules during mitotic spindle orientation, the authors proposed that GPSM2-GNAI similarly orients the migration of the basal body when post-mitotic HCs break planar symmetry. However, this hypothesis has not been validated *in vivo* to date. Studies where *Gpsm2* (Bhonker et al, 2016; Ezan et al, 2013; Tarchini et al, 2013), *Gnai3* (Beer-Hammer et al, 2018; Ezan et al, 2013) or *Gnai2; Gnai3* (Beer-Hammer et al, 2018) were inactivated did not report symmetrical HCs. In addition, mouse strains expressing ptxA *in vivo* also did not produce symmetrical cochlear HCs (Tarchini et al, 2013; Tarchini et al, 2016).

Second, ptx experiments induced striking HC misorientation. In the cochlea, misorientation manifested as a 180° inversion of outer HCs in the first and second row (OHC1-2) whereas inner HCs (IHCs) and OHC3 were much less affected (Figure 1B) (Ezan et al, 2013; Kindt et al, 2021; Tarchini et al, 2013). In vestibular organs, ptxA expression abrogated the line of polarity reversal and thus mirror-image HC organization in the maculae, the utricle and saccule (Jiang et al, 2017; Kindt et al, 2021). Similar defects were observed by inactivating two endogenous mouse proteins, the transcription factor EMX2 in the maculae (Jiang et al, 2017) and the orphan GPCR GPR156 in the cochlea and the maculae (Kindt et al, 2021). These recent studies uncovered an EMX2>GPR156>GNAI signaling cascade that regionally reverses HC orientation in macular organs to produce mirror-image HC organization. GNAI signals downstream of GPR156 to apparently reverse the orientation of basal body migration in *Emx2*-positive compared to *Emx2*-negative HCs (Tona & Wu, 2020) (reviewed in (Tarchini, 2021)). While ptx-induced HC misorientation is thus a physiologically relevant phenotype, HC misorientation was not reported in single *Gnai3* or double *Gnai2; Gnai3* mutants (Beer-Hammer et al, 2018; Mauriac et al, 2017).

In summary, the importance of the GPSM2-GNAI complex for hair bundle development is well-established, but multiple discrepancies cast a doubt on whether GNAI proteins also assume earlier polarization roles. Specific questions include whether GNAI proteins participate in the mechanism that pushes the basal body away from the cell center, and in the distinct EMX2>GPR156 mechanism that makes a binary decision on the direction of this push (Figure 1). Furthermore, it remains unclear whether GNAI2 and GNAI3 adopt similar or distinct distributions in HCs, and a potential role for GNAI1 or GNAO has not been addressed.

In this study, we embarked on a systematic analysis of single and combined *Gnai1*, *Gnai2*, *Gnai3* and *Gnao* mutants to solve the actual role(s) of GNAI proteins during HC differentiation. Our results show that GNAI3 is the only GNAI/O protein required for normal hair bundle morphogenesis and normal auditory brainstem response (ABR)

134 thresholds. In absence of GNAI3, GNAI2 can fully compensate at embryonic stages but
135 is not enriched with GPSM2 long enough to ensure normal hair bundle morphogenesis
136 at postnatal stages. We also directly demonstrate that GNAI proteins have two
137 polarization roles independent of GPSM2 during embryogenesis. In sum, GNAI function
138 is instrumental for HCs to a) break planar symmetry, b) adopt a proper binary
139 orientation along the PCP axis downstream of EMX2 and GPR156, and c) elongate and
140 organize stereocilia into a functional hair bundle with GPSM2.
141

142 **RESULTS**

143

144 **A near-comprehensive collection of *Gnai/o* mouse mutants**

145 In order to interrogate the individual and combined roles of all inhibitory G proteins
146 during HC differentiation, we obtained or generated mouse strains to build a collection
147 of single and double *Gnai/o* mutants. Single *Gnai1* and *Gnai3* mutants were derived
148 from the *Gnai1*^{tm1Lbi}*; Gnai3*^{tm1Lbi} double mutant strain (hereafter *Gnai1*^{neo}*; Gnai3*^{neo})
149 (Jiang et al, 2002) by segregating individual mutations upon breeding (see Methods and
150 Supp. Table 1 for details). We generated a new constitutive *Gnai2* mutant strain
151 (*Gnai2*^{del}) carrying a deletion of exons 2 to 4 (Figure 2 Supp. 1A; see Methods). Finally,
152 we obtained and derived two *Gnao1* mutant strains: a constitutive inactivation where a
153 neomycin cassette disrupts exon 6 (*Gnao1*^{neo}) (Jiang et al, 1998) and the consortium
154 alleles *Gnao1*$^{tm1c(EUCOMM)Hmgu}$ (conditional inactivation; hereafter *Gnao1*^{flox}*)*. As
155 simultaneous constitutive loss of GNAI1 and GNAI2 was reported as viable (Plummer et
156 al, 2012), we established a *Gnai1*^{neo}; *Gnai2*^{del} double mutant strain in addition to
157 *Gnai1*^{neo}*; Gnai3*^{neo} (Jiang et al, 2002). In contrast, double inactivation of *Gnai2; Gnai3* is
158 lethal around Embryonic (E) day 10.5, before HCs are born (Gohla et al, 2007).
159 Consequently, we generated a new *Gnai3*^{flox} strain by flanking exons 2 and 3 with *loxP*
160 sites (Figure 2 Supp.1B; see Methods). We then generated conditional *FoxG1-Cre;*
161 *Gnai2*^{del}*; Gnai3*^{flox} double mutants where *Gnai3* inactivation occurs as early as E8.5 in
162 the otic vesicle (Hebert & McConnell, 2000). Investigating all *Gnai/o* strains in the same
163 genetic background was unrealistic for feasibility and lethality reasons. We reasoned
164 that the key steps in HC apical differentiation we study are probably hardwired and less
165 likely to be influenced by genetic heterogeneity compared to susceptibility to disease,
166 for example.

167

168 As Pertussis toxin produced two of the three types of defects associated with GNAI/O
169 function (Figure 1B), *Gnai/o* strains above needed to be compared to a strain
170 expressing ptxA in HCs. We used our *R26*$^{LSL\text{-}myc:ptxA}$ strain (hereafter *LSL-myc:ptxA*)
171 expressing N-terminal myc-tagged ptxA after Cre-recombination (Tarchini et al, 2016).
172 Because a related *R26*$^{LSL\text{-}ptxAa:myc}$ strain carrying a C-terminal myc tag (Regard et al,

173 2007) caused much milder HC misorientation than *LSL-myc:ptxA* in the vestibular
174 system (Jiang et al, 2017; Kindt et al, 2021) , we questioned whether the myc tag could
175 weaken toxin activity even perhaps when located N-terminal. Consequently, we
176 generated a new strain, *R26*$^{DIO\text{-}ptxA}$ (hereafter *DIO-ptxA*), where untagged ptxA is
177 flanked by double-inverted *lox* sites and flipped from the non-coding to the coding
178 strand upon Cre recombination (Figure 2 Supp. 1C-D; see Methods) (Schnutgen et al,
179 2003). In *DIO-ptxA, ptxA* expression is driven by a strong artificial CAG promoter, and
180 not by the endogenous *R26* promoter as in previous strains (Regard et al, 2007;
181 Tarchini et al, 2016). We bred *LSL-myc:ptxA* and *DIO-ptxA* either with *FoxG1-Cre*
182 (Hebert & McConnell, 2000), or with *Atoh1-Cre* (Matei et al, 2005) to limit GNAI/O
183 inhibition to post-mitotic HCs. Supplementary Table 1 summarizes the strains used in
184 this study, their origin, genetic background and viability.
185

186 **Only GNAI3 is required for hair bundle morphogenesis yet other GNAI proteins**
187 **participate**

188 To investigate the role of individual GNAI/O proteins in HC development, we imaged
189 hair bundles in 3 week-old animals at mid-cochlear position using scanning electron
190 microscopy. In *Gnai3*^{neo} mutants, some OHC hair bundles appeared truncated, and
191 IHCs displayed variably shortened row 1 stereocilia as well as supernumerary
192 stereocilia rows (Figure 2A-C), as previously described (Mauriac et al, 2017). Single
193 inactivation of *Gnai1* or *Gnai2*, and double *Gnai1; Gnai2* inactivation did not produce
194 overt defects, yet quantifications revealed a subtle reduction in row 1 height in all cases
195 (Figure 2A, C). Accordingly, *Gnai1*^{neo}*; Gnai3*^{neo} double mutants appeared more severely
196 affected than single *Gnai3*^{neo} mutants: IHC row 1 height was further reduced (from
197 ~32% to ~47% reduced compared to littermate controls; Figure 2C), and the number
198 and width of row 1 stereocilia were respectively only significantly increased or
199 decreased in *Gnai1*^{neo}*; Gnai3*^{neo} mutants (Figure 2D-E). In contrast, a constitutive
200 (*Gnao1*^{neo}) or conditional (*Atoh1-Cre; Gnao1*^{flox}*)* inactivation of GNAO did not produce
201 overt apical HC defects, and conditional inactivation of GNAO did not enhance defects
202 in the *Gnai1*^{neo}*; Gnai3*^{neo} background (Figure 2 Supp. 1E-F).
203

204 As reported previously, *myc:ptxA* expression in post-mitotic HCs did not only stunt
205 stereocilia and produce extra rows, as seen in *Gnai3*^{neo} and *Gnai1*^{neo}*;Gnai3*^{neo} mutants
206 (Figure 2A-F), but also inverted OHC1-2 (Figure 2A) (Kindt et al, 2021; Tarchini et al,
207 2013; Tarchini et al, 2016). This defect was proposed to reflect an earlier role for GNAI
208 proteins downstream of the GPR156 receptor to define the binary orientation of HCs
209 along the PCP axis (Kindt et al, 2021). Despite breeding for over two years, we could
210 only obtain one single *Gnai2*^{neo}*; Gnai3*^{flox} adult double mutant due to postnatal lethality
211 (*FoxG1-Cre; Gnai2*$^{del/del}$*; Gnai3*$^{flox/flox}$; see Supp. Table 1). Remarkably, this specimen
212 recapitulated stereocilia stunting and extra rows observed in *Gnai3*^{neo},
213 *Gnai1*^{neo}*;Gnai3*^{neo} and *LSL-myc:ptxA* models (Figure 2A-F), but apparently also an
214 inversion of OHC1-2 only observed to date in *LSL-myc:ptxA* and *Gpr156* mutants
215 (Figure 2A; see also below, Figure 8 and Figure 8 Supp. 1) (Kindt et al, 2021). IHC
216 quantifications uncovered a *Gnai3*^{neo} < *Gnai1*^{neo}*; Gnai3*^{neo} < *LSL-myc:ptxA* < *FoxG1-*
217 *Cre; Gnai2*^{del}*; Gnai3*^{flox} allelic series along which a) defects increased in severity, as
218 manifested by increased variability and decreased averages (row 1 height and width;
219 Figure 2C-D), and b) new defects appeared (excess row 1 stereocilia in *Gnai1*^{neo}*;*
220 *Gnai3*^{neo} and more affected models; Figure 2E). In general, this phenotypic series
221 moves towards increasingly immature-looking hair bundles, and increasingly mimics
222 severe hair bundle defects in *Gpsm2* mutants (Mauriac et al, 2017; Tadenev et al, 2019;
223 Tarchini et al, 2016).
224
225 To quantify and compare hair bundle truncations in OHCs, we measured the length of
226 half-bundle 'wings' on each side of the central vertex and plotted paired left and right
227 values for each OHC (Figure 2G; Figure 2 Supp. 1G). We tested length variance using
228 mutant strains where hair bundles retained a recognizable vertex (thus excluding *LSL-*
229 *myc:ptxA* and *FoxG1-; Gnai2*^{del}*; Gnai3*^{flox} double mutants). In *Gnai1*^{neo}, *Gnai2*^{del} and
230 *Gnai1*^{neo}*; Gnai2*^{del} mutants, the two wings of each hair bundle had similar lengths and
231 variance was similar to control littermates. In contrast, variable truncation of one wing in
232 *Gnai3*^{neo} and *Gnai1*^{neo}*; Gnai3*^{neo} mutants resulted in significantly higher length variance
233 than controls (Figure 2G; Figure 2 Supp. 1G). In both *Gnai3*^{neo} and *Gnai1*^{neo}*; Gnai3*^{neo}

mutants, 49% of hair bundles had wings of more different lengths than the worst OHC outlier in littermate controls (see Source Data file).

In conclusion, GNAI proteins are not equally involved in hair bundle morphogenesis, with GNAI3 playing a particularly prominent role. GNAI2 makes a clear contribution since stereocilia defects increase in severity when GNAI loss extends from GNAI3 to both GNAI2 and GNAI3. These results confirm previous conclusions (Beer-Hammer et al, 2018). In addition, we largely rule out that GNAO is involved in apical HC differentiation, but uncover a possible contribution from GNAI1. Of note, as *Gnai3*^{neo} is in mixed (129S1/SvImJ; C57BL/6J) whereas *Gnai1*^{neo}*; Gnai3*^{neo} is in pure (129S1/SvImJ) genetic background (Supp. Table 1), we cannot rule out that the more severe defects in *Gnai1*^{neo}*; Gnai3*^{neo} double mutants originate from genetic modifiers in 129S1/SvImJ. Finally, the one adult specimen obtained for *FoxG1-Cre; Gnai2*$^{del/del}$*; Gnai3*$^{flox/flox}$ suggests that GNAI2 can fully compensate for the combined loss of GNAI1 and GNAI3 in *Gnai1*^{neo}*; Gnai3*^{neo} double mutants at embryonic stages, and secure proper OHC1-2 orientation in the EMX2>GPR156>GNAI signaling cascade. This important point is verified and expanded below where neonate HCs are analyzed.

Only GNAI3 is required for normal auditory brainstem thresholds yet other GNAI proteins participate

To pair morphological defects with auditory function, we next tested Auditory Brainstem Response (ABR) in mutants and control littermates at 3 to 4 weeks of age. Anesthetized animals were presented with pure tone stimuli of decreasing sound pressure intensity (dB SPL) at 8, 16, 32 and 40 kHz and ABRs were recorded with a subcutaneous probe (see Methods). Mirroring their overtly normal apical HC morphology, *Gnai1*, *Gnai2* and *Gnai1; Gnai2* mutants showed thresholds comparable to littermate controls at all frequencies (Figure 3A-C). Similarly, constitutive (*Gnao1*^{neo}) or conditional (*Atoh1-Cre; Gnao1*^{flox}) inactivation of GNAO did not alter ABR thresholds (Figure 3 Supp. 1A-B). In contrast, *Gnai3*^{neo} mutants were profoundly deaf at 32 and 40kHZ and displayed significantly elevated thresholds at 8 and 16 kHz compared to littermate controls (Figure 3D). *Gnai1*^{neo}*; Gnai3*^{neo} double mutants shared a similar ABR profile as *Gnai3*^{neo} single

265 mutants, with apparently higher thresholds at 8 and 16 kHz although these two strains
266 were not compared as littermates (Figure 3D). Littermate controls for *Gnai1*^{neo}*; Gnai3*^{neo}
267 double mutants were homozygote for *Gnai1*^{neo} (*Gnai1*$^{neo/neo}$*; Gnai3*$^{neo/+}$) and had
268 apparently higher thresholds than littermate controls for *Gnai3*^{neo} mutants (*Gnai3*$^{neo/+}$)
269 whereas loss of GNAI1 did not impact auditory thresholds on its own (Figure 3A). These
270 results match more severe hair bundle defects when GNAI1 is inactivated along with
271 GNAI3 (Figure 2C-F), and here again, could reflect either a limited role for GNAI1 in
272 hearing or differences in genetic background.
273
274 In summary, we confirm that GNAI3, but not GNAI2, is essential for proper auditory
275 thresholds, as previously proposed (Beer-Hammer et al, 2018). We raise the possibility
276 that GNAI1 may have a limited role, and clarify that GNAO does not participate. Beer-
277 Hammer and colleagues previously showed that inactivating GNAI2 worsens hearing
278 loss in the *Gnai3* null background, as tested in *FoxG1-Cre; Gnai2*$^{flox/flox}$*; Gnai3*$^{flox/flox}$
279 adults (Beer-Hammer et al, 2018). Using a comparable yet distinct model (*FoxG1-Cre;*
280 *Gnai2*$^{del/del}$*; Gnai3*$^{flox/flox}$), we were largely unable to obtain young adults and thus could
281 not perform ABR. This suggests that our model is more severely affected, and probably
282 lacks ABRs similar to the *FoxG1-Cre; Gnai2*$^{flox/flox}$*; Gnai3*$^{flox/flox}$ (Beer-Hammer et al,
283 2018) and *LSL-myc:ptxA* (Tarchini et al, 2016) models.
284
285 **Distribution of individual GNAI proteins in neonate hair cells**
286 Next, we attempted to detect individual GNAI/O proteins in neonate HCs and define
287 how they localize. Because GNAI/O proteins are close paralogs, validating and using
288 specific antibodies is challenging. Instead, we used one commercial antibody raised
289 against GNAI3 (scbt"GNAI3"; expected to detect GNAI3>GNAI1>GNAI2) and one
290 antibody raised against GNAI2 (pt"GNAI2"; expected to detect GNAI2>GNAI1>GNAI3;
291 see Methods) and systematically immunolabeled our collection of mouse models to
292 tease apart protein-specific behavior.
293
294 Both antibodies produced the familiar GNAI pattern of enrichment at the bare zone and
295 at row 1 stereocilia tips (Figure 4) (Tarchini et al, 2013; Tarchini et al, 2016). Both

296 revealed generally normal GNAI enrichment in *Gnai1*^{neo} (Figure 4A), *Gnai2*^{del} (Figure
297 4B), and *Gnai1*^{neo}; *Gnai2*^{del} double mutants (Figure 4C). This indicates that pt"GNAI2" is
298 not specific for GNAI2, can also detect GNAI3, and should thus be able to detect
299 GNAI1, a better target than GNAI3. In *Gnai3*^{neo} single and *Gnai1*^{neo}*; Gnai3*^{neo} double
300 mutants, both antibodies still revealed GNAI protein at the bare zone and at stereocilia
301 tips although some HCs displayed incomplete enrichment (Figure 4D-E; further detailed
302 below). This indicates that scbt"GNAI3" is not specific for GNAI3, can also detect
303 GNAI2, and should thus be able to detect GNAI1, a better target than GNAI2. Finally,
304 neither antibody detected consistent signal over background in *Gnai2; Gnai3* double
305 mutants (Figure 4F; *FoxG1-Cre; Gnai2*$^{del/del}$*; Gnai3*$^{flox/flox}$). Together, these results
306 indicate that a) GNAI2 and GNAI3 share the same polarized distribution pattern at the
307 bare zone and at stereocilia tips, and b) GNAI1 is either present in very low amounts
308 hidden by background signal, or absent at the HC apical surface. Loss of GNAO in the
309 *Gnao1*^{neo} or *Atoh1-Cre; Gnao1*^{flox} models did not alter signals obtained with
310 scbt"GNAI3" (Figure 4 Supp. 1A-B). Moreover, a GNAO antibody produced unpolarized
311 apical signals that we deemed unspecific because they were unchanged in *Atoh1-Cre;*
312 *Gnao1*$^{flox/flox}$ mutants (Figure 4 Supp. 1C). GNAO thus likely does not contribute to HC
313 polarization, as also suggested by normal hair bundles and normal ABR thresholds in
314 *Gnao1* mutants.
315

316 **GNAI2 only partially spans the bare zone and stereocilia tips and partially rescues**
317 **hair bundle development in postnatal hair cells lacking GNAI3**

318 We next took a closer look at incomplete GNAI enrichment in *Gnai3*^{neo} and *Gnai1*^{neo}*;*
319 *Gnai3*^{neo} mutant HCs (Figure 4D-E). In both models, we observed an identical outcome
320 at the P0 cochlear base where remaining GNAI was unable to fully and consistently
321 occupy the HC sub-domains where GNAI3 was missing (Figure 5A-B; bare zone,
322 arrows; stereocilia tips, arrowheads). In *Gnai1*^{neo}*; Gnai3*^{neo} double mutants (Figure 5B),
323 the GNAI protein detected is by default GNAI2 and, based on results above (Figure 4),
324 we conclude that GNAI2 likely also forms the bulk of remaining GNAI in *Gnai3*^{neo}
325 mutants (Figure 5A). Because in all cases GPSM2 co-localized with GNAI2 (Figure 5A-
326 B), these results demonstrate that GNAI2, and not only GNAI3, can form a complex with

327 GPSM2 in HCs. Intriguingly, the absence of GPSM2-GNAI2 on one side of the bare
328 zone at P0 appeared to coincide with its absence at stereocilia tips on the
329 corresponding side (Figure 5A-B). We thus quantified GNAI2 intensity at the bare zone
330 and at stereocilia tips in half-OHCs in *Gnai1*$^{neo;}$ *Gnai3*^{neo} mutants. While as expected
331 control OHCs showed little variation in GNAI enrichment in either compartment (Figure
332 5 Supp. 1A), mutant OHCs showed highly variable signals that were significantly
333 correlated between the bare zone and tips in the same half-OHC (Figure 5C). Analyzing
334 HCs at different stages and tonotopic positions (gradient of increasing HC maturity from
335 cochlear apex to base) clarified that GNAI2 is progressively unable to compensate for
336 missing GNAI3. At E18.5, the GPSM2-GNAI2 complex could still occupy the totality of
337 the bare zone in *Gnai1*$^{neo;}$ *Gnai3*^{neo} mutants (Figure 5 Supp. 1B), suggesting that GNAI2
338 fully compensates for the loss of GNAI3 in embryonic HCs. Partial complementation by
339 GNAI2 observed at P0 (Figure 5A-C) evolved into a lack of complementation at P6 at
340 the cochlear base, where GNAI2 was no longer detected at the tips of stunted
341 stereocilia in mutant IHCs (Figure 5D). In contrast, more immature P6 IHCs at the
342 cochlear mid position retained partial GNAI2 enrichment correlated between the bare
343 zone and tips (Figure 5E), as seen at P0 (Figure 5A-B). Time and position-based
344 differences suggest that GNAI2 is progressively unable to occupy the full bare zone and
345 tip compartments during HC differentiation.
346
347 The progressive inability of GNAI2 to cover for GNAI3 in individual HCs helps explain
348 the unique profile of apical surface defects in *Gnai3*^{neo} and *Gnai1*$^{neo;}$ *Gnai3*^{neo} mutant
349 HCs. Loss of GPSM2-GNAI2 in one wing of the OHC hair bundle led to stereocilia
350 degeneration by P8 (Figure 5F). One-sided loss of global GNAI function at stereocilia
351 tips is thus likely the origin of truncated hair bundle wings observed in adults *Gnai3*^{neo}
352 and *Gnai1*$^{neo;}$ *Gnai3*^{neo} mutant OHCs (Figure 2G). We divided the P8 OHC apical
353 surface in two halves based on the position of the basal body at the hair bundle vertex,
354 and measured the length of each hair bundle wing as well as the total apical surface
355 area in the same half in *Gnai1*^{neo}*; Gnai3*^{neo} mutants (Figure 5F). We found a significant
356 correlation between these two values (Figure 5G; control graph in Figure 5 Supp. 1C),
357 providing new evidence that loss of stereocilia prompts a corresponding loss of flat HC

surface area on the same OHC side (Etournay et al, 2010). Finally, we asked whether in time GNAI2 is lost at all stereocilia tips and along the entire cochlea in *Gnai1*$^{neo;}$ *Gnai3*^{neo} mutants. This proved not to be the case, as GNAI2 could still be detected at stereocilia tips in P28 OHCs and IHCs, although in low and variable amounts compared to GNAI tip signals in littermate controls (Figure 5 Supp. 1D-E).

In conclusion, GNAI2 still provides a low dose of GNAI protein at the tip of stereocilia that do not degenerate when GNAI3 is missing. Variable GNAI2 amounts likely explain why IHCs stereocilia have variably reduced heights in absence of GNAI3 (Figure 2B-C; Figure 5D-E), unlike in *Gpsm2* or *LSL-myc:ptxA* mutants where they are more uniformly stunted (Beer-Hammer et al, 2018; Mauriac et al, 2017; Tadenev et al, 2019; Tarchini et al, 2016). Interestingly, correlated loss of GNAI2 signal at the bare zone and at stereocilia tips on the same HC side adds to previous evidence suggesting that bare zone enrichment is essential for GPSM2-GNAI transfer to adjacent row 1 stereocilia (Akturk et al, 2022; Jarysta & Tarchini, 2021; Tarchini et al, 2016).

Combined loss of GNAI2 and GNAI3 delays and de-polarizes bare zone expansion with drastic consequences on stereocilia distribution

Since GNAI2 and GNAI3 show functional redundancy and are the most important GNAI/O proteins for hair bundle differentiation, we next focused on characterizing early HC development in *Foxg1-Cre; Gnai2*$^{del/del}$*; Gnai3*$^{flox/flox}$ mutants and comparing defects to those observed previously with Pertussis toxin. Unlike at adult stage, *Gnai2; Gnai3* double mutants were obtained in close to Mendelian proportion at P0. For this purpose, we used the new *DIO-ptxA* allele in case the myc tag hindered ptxA activity in the *LSL-myc:ptxA* allele. We started with validating the new *Gnai3*^{flox} *and DIO-ptxA* alleles (Figure 2 Supp. 1B-C). As expected, GNAI signals at the bare zone and stereocilia tips were normal in *Gnai3*$^{flox/flox}$ homozygotes but showed a distinctive incomplete pattern along with stunted stereocilia upon Cre recombination (Figure 6 Supp. 1A), as in constitutive mutants (Figure 5A). The new *DIO-ptxA* model produced in fact identical apical HC defects to the earlier *LSL-myc:ptxA* strain in single HCs (Kindt et al, 2021; Tarchini et al, 2016) (Figure 6 Supp. 1B). The fraction of inverted OHC1 in the *DIO-ptxA*

389 model was lower than in the *LSL-myc:ptxA* model when using the later *Atoh1-Cre*
390 (Figure 6 Supp. 1C-D), but identically encompassed 100% of OHC1 with *FoxG1-Cre*.
391 Similar apical HC defects between strains indicate that the N-terminal myc and mild *R26*
392 promoter do not limit ptxA activity in *LSL-myc:ptxA*. For comparison purposes, we used
393 the *FoxG1-Cre* driver to inactivate GNAI2/GNAI3 and to express ptxA, the same driver
394 used by Beer-Hammer and colleagues (Beer-Hammer et al, 2018).
395
396 Inactivating GNAI2 and GNAI3 abolished the bare zone at E17.5 based on the absence
397 of GNAI labeling that was obvious in controls, and abnormally uniform F-actin signals at
398 the HC surface (Figure 6A-B; arrows point to the bare zone). In contrast, E17.5 *DIO-*
399 *ptxA* HCs had developed a distinct bare zone (Figure 6C, arrows). Measuring its surface
400 area by HC type confirmed that the bare zone is virtually absent in conditional *Gnai2;*
401 *Gnai3* double mutants and reduced in ptxA-expressing OHCs but not IHCs (Figure 6D).
402 By P0, most *Gnai2; Gnai3* mutant HCs at the cochlear base had developed a region
403 lacking microvilli or stereocilia, but its position at the apical surface was highly irregular,
404 complementing extremely dysmorphic hair bundles (Figure 6E-F; arrows point to bare
405 regions). In contrast, P0 *DIO-ptxA* HCs displayed largely coherent hair bundles and a
406 distinct bare zone (Figure 6G, arrows). Quantifications revealed a significantly reduced
407 bare area in P0 *Gnai2; Gnai3* mutants compared to littermate controls (Figure 6H),
408 showing that bare zone emergence and expansion is greatly delayed and deregulated
409 in this model (compare P0 in Figure 6H and E17.5 in Figure 6D). In line with delayed
410 bare zone expansion upon inhibiting GNAI function, bare zone surface area was back to
411 normal in P0 *DIO-ptxA* HCs, except in the least mature OHC3 (compare P0 in Figure
412 6H and E17.5 in Figure 6D).
413
414 These results best illustrate to date the importance of GPSM2-GNAI for bare zone
415 emergence, expansion and polarized positioning. While both mutant models
416 consistently delay bare zone expansion, differences in timing and severity suggest that
417 ptxA expression does not achieve as extended a loss of GNAI function as the *Gnai2;*
418 *Gnai3* double mutant. This is further underscored by severe stereocilia distribution
419 defects observed in *Gnai2; Gnai3* but not *DIO-ptxA* mutants. As reported previously

420 (Kindt et al, 2021; Tarchini et al, 2013; Tarchini et al, 2016), the orientation of OHC1-2
421 expressing ptxA was reversed compared to controls (Figure 6C, G), and we expected to
422 observe a similar pattern of misorientation in *Gnai2; Gnai3* mutants. However, HC
423 orientation proved challenging to assess in *Gnai2; Gnai3* mutants due to highly
424 dysmorphic hair bundles (Figure 6A-B; E-F). We used acetylated tubulin (AcTub) and
425 pericentrin (PCNT) as markers for the kinocilium and the position of the basal body,
426 respectively. This showed that in *Gnai2; Gnai3,* but not in *DIO-ptxA* mutants, the basal
427 body and kinocilium were sometimes in an approximately central position surrounded
428 partially or entirely by stereocilia (Figure 6E-F). Rounded perinatal hair bundles are a
429 hallmark of HCs where the early off-center migration of the basal body, hence symmetry
430 breaking, is defective.
431
432 To distinguish defects affecting symmetry-breaking versus HC orientation and to
433 uniformize analysis of HC polarization, we next used the position of the basal body at
434 the base of the kinocilium to derive both HC eccentricity and HC orientation. This
435 strategy helped compare the two mouse models, and identified two early functions for
436 GNAI before its association with GPSM2 for stereocilia elongation.
437
438 **GNAI proteins drive the off-center migration of the basal body**
439 We used the position of the basal body to measure HC eccentricity as a metric for
440 cytoskeleton asymmetry. Eccentricity was calculated as a ratio reporting how far away
441 from the cell center the basal body was positioned (see schematic in Figure 7). A
442 perfectly symmetrical HC with a central basal body would thus have an eccentricity ratio
443 close to 0 whereas a ratio close to 1 would indicate that the off-center basal body is
444 juxtaposed to the apical junction. Because HC maturation progresses in time and along
445 the tonotopic axis (cochlear apex to base gradient of increasing maturity), we measured
446 eccentricity at E17.5 (base and mid cochlear position) and at P0 (base, mid and apex)
447 to understand how eccentricity progressed at the HC population level.
448 Control HCs at E17.5 had already broken symmetry at the mid position, with eccentricity
449 averaging ~0.5 and increasing at the more mature base position (Figure 7A). At E17.5
450 mid and base positions, *Gnai2; Gnai3* mutants showed significantly reduced

451 eccentricity, suggesting a delay in the off-center migration of the basal body. We
452 arbitrarily defined 0.25 as a threshold below which HCs were considered “symmetrical”.
453 Symmetrical HCs were not observed in controls but represented up to ~29% of IHCs
454 and ~34% of OHCs in mutants at E17.5 (detailed in Figure 7A by stage, position and
455 HC type, red highlights). By P0, the proportion of symmetrical cells in mutants had
456 decreased at all positions for OHCs (3-15%), but remained high for IHCs (21.5%; Figure
457 7A). P0 OHC eccentricity generally remained lower in mutants than in controls, with a
458 trend towards less significant differences in OHCs at the cochlear base where HCs are
459 most mature. In contrast, IHCs did not appear to recover by P0, as eccentricity was
460 much lower than in controls, even at the cochlear base.
461
462 The situation was radically different in the *DIO-ptxA* model. First, no symmetrical HC
463 was observed at any stage or position in mutants (Figure 7B). In fact, eccentricity was
464 instead higher in *DIO-ptxA* OHCs compared to littermate controls, with a tendency for
465 this difference to become less significant along with OHC differentiation (see below for
466 interpretation). IHCs had overall a normal distribution of eccentricity compared to
467 controls in the *DIO-ptxA* model.
468
469 Defects in bare zone expansion (Figure 6D, H) can help explain the distinct eccentricity
470 defects in the *DIO-ptxA* and *Gnai2; Gnai3* mouse models. At E17.5 and P0, the position
471 of the basal body is the sum of two opposite movements (Figure 1A): a) the early off-
472 center migration that brings it in the vicinity of the lateral junction, and b) the subsequent
473 relocalization towards the cell center that brings it in contact with the forming hair bundle
474 upon bare zone expansion (Tarchini et al, 2013). In *DIO-ptxA*, we interpret transiently
475 increased eccentricity in OHCs (Figure 7B) as the outcome of normal off-center basal
476 body migration yet delayed bare zone expansion (Figure 6D, H). In *Gnai2; Gnai3*
477 mutants, however, decreased eccentricity in OHCs (Figure 7A) stems from defective
478 basal body off-center migration compounded with a first absent (E17.5), and then
479 reduced (P0), bare region (Figure 6D, H). When an unpolarized bare region eventually
480 emerges in *Gnai2; Gnai3* mutants (Figure 6H), it impacts basal body position without
481 directionality, leading to highly variable eccentricity values compared to controls (Figure

482 7A), and thus variably dysmorphic hair bundles. The apparent increase in symmetrical
483 IHCs over time in *Gnai2; Gnai3* mutants (Figure 7A) may result from the delayed
484 expansion of the bare region, which will relocalize the basal body centrally in a
485 proportion of IHCs.
486
487 In conclusion, the loss of GNAI activity achieved in *Gnai2; Gnai3* mutants impairs
488 symmetry-breaking (Figure 7) before it impairs bare zone emergence and expansion
489 (Figure 6). PtxA-based downregulation of GNAI activity is sufficient to delay bare zone
490 expansion, but not to affect symmetry-breaking. As only ~3-15% of OHCs and ~21% of
491 IHCs in *Gnai2; Gnai3* mutants are symmetrical at the P0 cochlear base, there is likely
492 sufficient GNAI activity remaining in this model as well for most HCs to break planar
493 symmetry.
494
495 **GNAI proteins orient hair cells laterally**
496 GNAI proteins were proposed to signal downstream of the GPR156 receptor to regulate
497 HC orientation in the auditory and vestibular organs (Jiang et al, 2017; Kindt et al,
498 2021). In HCs expressing the transcription factor EMX2, GPR156 reverses the
499 orientation of the off-center basal body migration, and thus HC orientation, compared to
500 *Emx2*-negative HCs (Tona & Wu, 2020). To date, however, the HC misorientation
501 profile observed in *Emx2* or *Gpr156* mutants was only recapitulated using ptxA (Figure
502 1B). If ptxA-based orientation defects are physiologically relevant to GNAI function, they
503 should be observed in *Gnai2; Gnai3* mutants that achieve a further loss of GNAI activity.
504
505 To test this assumption, we first excluded symmetrical HCs (eccentricity< 0.25) in the
506 E17.5 and P0 datasets since an asymmetric cytoskeleton is pre-requisite for HCs to
507 exhibit a defined orientation. Next, we used the position of the off-center basal body in
508 the remaining HCs to infer their orientation. We measured the angle formed by a vector
509 running from the HC center to the basal body relative to the cochlear longitudinal axis
510 (α, see schematic in Figure 8). Angles were plotted in circular histograms where 0°
511 pointed to the cochlear base along the longitudinal axis, and 90° to the lateral edge.
512

513 At E17.5 at the cochlear mid position, *DIO-ptxA* already showed the graded pattern of
514 OHC misorientation described previously, with inverted OHC1-2 and imprecisely
515 oriented IHCs and OHC3 (Figure 8A). At this stage and position, *Gnai2; Gnai3* mutant
516 HCs above threshold showed abnormal and highly variable orientations without a clear
517 trend towards OHC1-2 inversion yet. Strikingly however, more mature E17.5 OHC1 at
518 the base were largely inverted (Figure 8B), as also observed at P0 at all positions
519 (Figure 8C-D; Figure 8 Supp. 1A). OHC2 were still largely oriented laterally at the E17.5
520 mid (Figure 8B) and P0 apex and mid (Figure 8C; Figure 8 Supp. 1A), but clearly
521 adopted an inverted medial orientation at the P0 base (Figure 8D). These results thus
522 confirm for the first time that endogenous GNAI proteins are integral to proper HC
523 orientation. They also clarify that the level of GNAI activity required for proper HC
524 orientation is higher than for symmetry-breaking since both *DIO-ptxA* and *Gnai2; Gnai3*
525 mutants showed HC misorientation. It should be noted that concomitant deficits in HC
526 eccentricity and the arbitrary eccentricity cut-off at 0.25 were expected to blur the
527 misorientation pattern, explaining why OHC1-2 inversion only becomes apparent at later
528 stages of differentiation in *Gnai2; Gnai3* compared to *DIO-ptxA* mutants. Interestingly,
529 unlike in *DIO-ptxA* mutants, IHC and OHC3 were also severely misoriented in *Gnai2;*
530 *Gnai3* mutants at all stages and positions analyzed (Figure 8; Figure 8 Supp. 1A). We
531 thus conclude that a lower level of GNAI activity is sufficient to properly orient IHC and
532 OHC3 compared to OHC1-2 (see Model Figure 9).

533 **DISCUSSION**

534

535 By examining a large collection of single and combined mutations in *Gnai* genes (*Gnai1*,
536 *Gnai2*, *Gnai3*, *Gnao1*), we assign here three distinct and successive roles for GNAI
537 proteins during the apical polarization of a developing HC (Figure 9): a) drive the
538 centrifugal migration of the basal body when a prospective HC breaks planar symmetry,
539 b) orient this migration along the PCP axis in a binary manner, and c) position and
540 elongate stereocilia during hair bundle morphogenesis. Key results in the study include
541 demonstrating that endogenous GNAI proteins indeed serve early functions (a) and (b),
542 since to date only hair bundle defects (c) were reported in knock-out mouse models
543 where *Gnai* genes were directly targeted (Beer-Hammer et al, 2018; Mauriac et al,
544 2017). Importantly, previous studies indicated that GNAI proteins partner with different
545 regulators in these different functions, organizing and elongating stereocilia by binding
546 to the scaffold GPSM2 (c), and reversing HC orientation in *Emx2*-expressing HCs via
547 heterotrimeric signaling downstream of the GPR156 receptor (b). A GNAI regulator or
548 mechanism for basal body off-center migration (a) remains to be identified.

549

550 **Different GNAI/O identity, dosage and timing underlie different functions**

551 Interestingly, besides involving different regulators, each function also involves different
552 dosage and specific identity of the underlying GNAI protein(s) at different times during
553 HC development (Figure 9). For postnatal hair bundle morphogenesis (c), GNAI
554 proteins are sequestered in the GDP state by GPSM2, forming a complex highly
555 enriched at the bare zone and at row 1 stereocilia tips that can be reliably
556 immunodetected (Akturk et al, 2022; Kindt et al, 2021). In these two sub-cellular
557 compartments, the identity of the GNAI proteins at work appears to matter, with GNAI3
558 playing a necessary and prominent role while GNAI2 is important yet not required. We
559 cannot rule out that GNAI1 participates as well in a minor way because *Gnai1* mutants
560 appear to have more variable stereocilia height than littermate controls (Figure 2C), and
561 we observed more severe stereocilia defects and more elevated ABR thresholds in
562 *Gnai1; Gnai3* compared to single *Gnai3* mutants (Figure 2C, E; Figure 3D). The latter
563 observations might instead reflect differences in the genetic background, however. In

stark contrast, GNAI2 can fully rescue normal off-center basal body migration (a) and normal HC orientation (b) when both GNAI1 and GNAI3 are constitutively absent (Figure 9). In *FoxG1-Cre; Gnai2; Gnai3* double mutants, a majority of HCs eventually break symmetry, strongly suggesting that GNAI1 and/or GNAO can participate in the off-center migration mechanism. Finally, even high expression of untagged ptxA in the *DIO-ptxA* model does not affect symmetry-breaking in cochlear HCs, whereas ptxA severely disrupts HC orientation (Figure 9). We thus conclude that i) ptxA downregulates but does not abolish GNAI/O activity in HCs, and ii) the GNAI dosage required to ensure each function is graded (a)<(b)<(c), with probably several GNAI/O proteins able to participate in embryonic functions (a, b). A low dose of GNAI/O dynamically cycling between the GDP and GTP-bound state in heterotrimeric G protein complexes could explain why GNAI proteins are not immunodetected along with GPR156 or other regulators besides GPSM2 (Akturk et al, 2022; Kindt et al, 2021).

A strict dosage- and time-dependence for correct GNAI functions explains why our conditional *Gnai2; Gnai3* double mutant model is more severely affected than a comparable conditional *Gnai2; Gnai3* model where only hair bundle defects (c) were reported (Beer-Hammer et al, 2018). While Beer-Hammer and colleagues used *FoxG1-Cre* as a driver as we did, combined GNAI2 and GNAI3 inactivation demanded Cre recombination at four floxed loci (*Gnai2*$^{flox/flox}$*; Gnai3*$^{flox/flox}$). In contrast, our model demands recombination at two loci only (*Gnai2*$^{del/del}$*; Gnai3*$^{flox/flox}$). We thus conclude that our model achieves an earlier and greater loss of GNAI activity. This explanation is supported by extensive perinatal lethality in our model, whereas Beer-Hammer and colleagues could analyze *Gnai2; Gnai3* double mutants as adults. Our work thus usefully reconcile all previous reports about GNAI functions, notably showing that inactivating endogenous GNAI proteins does produce early defects (a,b) so far only observed with ptx. We also validate all HC defects observed with ptx as physiologically relevant and specific to GNAI/O function.

Hair cell break of symmetry

Although cochlear HCs expressing ptxA undergo normal symmetry-breaking in vivo (Kindt et al, 2021; Tadenev et al, 2019; Tarchini et al, 2013; Tarchini et al, 2016), a fraction of HCs expressing ptxA in the utricle and saccule have abnormally central basal bodies (Kindt et al, 2021). This suggests that a higher dose of GNAI is required for off-center migration of the basal body in vestibular compared to cochlear HCs, making vestibular HCs more susceptible to ptxA. “Ciliary” proteins are required for ciliogenesis, including kinocilium formation and maintenance, and also play non-ciliary functions (May-Simera et al, 2015; Sipe & Lu, 2011). Inactivation of intraflagellar transport protein IFT88 was reported to result in a central basal body and circular hair bundles in ~10% of OHCs (Jones et al, 2008), but the underlying mechanism was not elucidated. A low proportion of symmetrical HCs were also reported in absence of the CD2 isoform of the protocadherin PCDH15 that forms inter-stereocilia and kinocilium-stereocilia fibrous links during embryogenesis (Webb et al, 2011). It remains unclear whether GNAI activity is involved or not in *Ift88* or *Pcdh15* mutant defects, or whether GNAI could be active at the basal body or the kinocilium.

Hair cell orientation

The PCP axis is defined by opposite asymmetric enrichment of the core PCP transmembrane proteins VANGL2 and FZD3/6 and their specific cytosolic partners at HC apical junctions (Deans, 2013; Montcouquiol & Kelley, 2019; Tarchini & Lu, 2019). Previous work showed that regional *Emx2* expression in HCs reverses how the basal body migrates relative to early-set core PCP landmarks, establishing the line of polarity reversal in the utricle and saccule (Jiang et al, 2017; Tona & Wu, 2020). EMX2 activates the GPCR GPR156 by triggering its polarized enrichment at the apical HC junction, where downstream GNAI signaling appears to repel the basal body (Figure 9, b) (Kindt et al, 2021). It is important to note that HCs lacking GPR156 have a normal apical cytoskeleton, including a normally formed hair bundle, and only show orientation defects (Kindt et al, 2021). This indicates that the centrifugal move of the basal body and the orientation of this move that defines early HC orientation are two distinct molecular mechanisms that both involve GNAI/O proteins (Figure 9; a-b). HC orientation is regulated by core PCP proteins defining an axis of polarization, and by the

625 EMX2>GPR156>GNAI cascade defining binary orientation along that axis. Following
626 the same logic, HCs lacking GPSM2 are not inverted in orientation as in *Emx2*, *Gpr156*,
627 *Gnai2; Gnai3* or *ptxA* mutants (Bhonker et al, 2016; Ezan et al, 2013; Tarchini et al,
628 2013). This shows that bare zone enrichment of GPSM2-GNAI is a mechanism to
629 shape and polarize the growth of the hair bundle, but not to migrate off-center or orient
630 the basal body. It is worth noting that GPSM2-GNAI is polarized at the HC apical
631 membrane on the side of the off-center basal body, and not at the apical junction where
632 core PCP proteins regulate HC orientation (Siletti et al, 2017; Tarchini et al, 2013).
633
634 While both GPR156 (Greene et al, 2023) and GPSM2 (Doherty et al, 2012; Walsh et al,
635 2010) have been reported as human deafness genes, there is currently no evidence
636 implicating any GNAI/O protein. This is most likely because even GNAI3, which is more
637 specifically required for hair bundle morphogenesis (Figure 9), plays ubiquitous and
638 critical signaling roles in the context of heterotrimeric protein signaling across many cell
639 types.
640

641 **METHODS**

642

643 **Mouse strains and husbandry**

644 All mouse strains used in this work and strain-related information is summarized in
645 Supplementary Table 1. All primers used for genotyping are indicated in Supplementary
646 Table 2 by strain.

647 Strains from The Jackson Laboratory: *Gnai1*^{neo}*; Gnai3*^{neo} (*Gnai1*^{tm1Lbi}*; Gna3*^{tm1Lbi}*;* MGI:
648 5560183) (Jiang et al, 2002) carries a neo cassette in *Gnai1* exon 3 and a neo cassette
649 replacing part of intron 5 and exon 6 in *Gnai3* in the 129S1/SvImJ background. The
650 single *Gnai1*^{neo} and single *Gnai3*^{neo} alleles were segregated from *Gnai1*^{neo}*; Gnai3*^{neo} by
651 breeding with C57BL/6J mice and are consequently on a mixed 129S1/SvImJ:
652 C57BL/6J background. *Gnao1*^{neo} (*Gnao1*^{tm1Lbi}; MGI: 2152685) carries a neo cassette in
653 *Gnao1* exon 6 in the 129S1/SvImJ background (Jiang et al, 2002). The two *Cre* strains
654 used in this work are *Atoh1-Cre* (*Tg(Atoh1-cre)1Bfri;* MGI: 3775845) expressing Cre in
655 HCs from E14.5 (Matei et al, 2005) and *FoxG1-Cre* (*Foxg1*$^{tm1(cre)Skm}$; MGI: 1932522)
656 expressing Cre in the prospective otic vesicle from E8.5 (Hebert & McConnell, 2000).

657

658 Consortium strain: *Gnao1*^{flox} (*Gnao1*$^{tm1c(EUCOMM)Hmgu}$) is a derivative of the EUCOMM
659 strain *Gnao1*$^{tm1a(EUCOMM)Hmgu}$ (MGI: 4456727; "KO first, conditional ready"). The *Gnao1*^{flox}
660 conditional allele was produced via FLP-mediated recombination (FLP strain MGI:
661 4830363) to remove the FRT-flanked *LacZ-neo* cassette, leaving exon 3 floxed.
662 *Gnao1*^{flox} is on a C57BL/6N background.

663

664 Constitutive *Gnai2*^{del} inactivation (see Figure 2 Supp. 1A). *Gnai2*^{del} (*Gnai2*$^{em1Btar;}$ MGI:
665 6466534) was generated using direct delivery of CRISPR-Cas9 reagents in mouse
666 zygotes via electroporation. The following guide RNAs (gRNA) were used to delete
667 exon 2, exon 3 and part of exon 4 in the C57BL/6J background. Upstream gRNA:
668 CTGCCCTCTGTTCCAGGTGC, downstream gRNA: ATGCTTCCTGAAGACCTGTC.
669 The resulting 681 bp deletion encompassed
670 TGCTGGAGAGTCAGGGAAGA...CCTGAAGACCTGTCCGGTGT. The electroporation
671 mixture consisted of the gRNAs with AltR- *Streptococcus pyogenes* Cas9 (SpCas9) V3

672 (Integrated DNA Technologies #1081059) in embryo-tested TE buffer (pH 7.5).
673 Electroporation of zygotes was performed as described in (Qin et al, 2015). In order to
674 segregate away potential non-specific mutations, founders were bred for two
675 generations with C57BL/6J animals to generate a N2 heterozygote stock. Because
676 *Gnai2*^{del} homozygotes showed low viability, this strain was used in a mixed
677 C57BL/6J:FVB/J background that improved the proportion of homozygotes (see Supp.
678 Table 1).
679
680 Conditional *Gnai3*^{flox} inactivation (see Figure 2 Supp. 1B). A plasmid-based donor
681 vector was cloned to flank *Gnai3* exon 2 and 3 with *loxP* sites using the same
682 CRISPR/Cas9 system described above for *Gnai2*$^{del.}$ A fragment carrying a *loxP*, a
683 genomic region including exon 2-3, the restriction site ClaI, a second *loxP* and the
684 restriction site XhoI was synthetized (Genscript) and cloned between 5' and 3' homology
685 arms amplified by PCR using Gibson assembly. The following gRNAs were used and
686 define the extremities of the floxed region: upstream, AGCTCACCAAAATTCCCATT,
687 TAGGGGATATAGATCCAAAT, downstream, TTCCAGGACTCTGCATGCGT,
688 TACCGACGCATGCAGAGTCC. The gene editing reagents (gRNAs, donor vector,
689 SpCas9) were microinjected in zygotes as described in (Qin et al, 2015). To confirm
690 insertion at the *Gnai3* locus, we performed long-range PCRs with a genomic primer
691 located outside the homology arm on each side: *5' long-range:* F(external)_
692 TACTGAGATGAGAGACTGAGGG and R (internal)_TGGCTGACATCCTTTGATGGAC.
693 The 3070 bp product was digested with XhoI, producing 2,551 + 519 bp fragments upon
694 donor insertion (flox allele). 3' long-range: F
695 (internal)_TGAAAGGTAAAGGCAACGTGAG and R
696 (external)_TGTGAGACAGGGTCTCTCTTTG. The 2,966 bp product was digested with
697 XhoI, producing 2,000 + 966 bp fragments upon donor insertion (flox allele). In order to
698 segregate away potential non-specific mutations, founders were bred for two
699 generations with C57BL/6J animals to generate a N2 heterozygote stock.
700
701 Pertussis toxin catalytic subunit (ptxA)-expressing strains (see Figure 2 Supp. 1C-D).
702 The *LSL-myc:ptxA* strain at the *ROSA26* (*R26*) locus was described previously

703 (*Gt(ROSA)26Sor*$^{em1(ptxA)Btar}$; MGI: 6163665) (Tarchini et al, 2016). The new *CAG-DIO-*
704 *ptxA* strain line (see Figure 2 Supp. 1C) was generated at the *R26* locus using the Bxb1
705 attP(GT) integrase technology and *C57BL/6J-Gt(ROSA)26Sor*$^{<em2Mvw>/Mvw}$ (MGI:
706 6757188) as the host strain (Low et al, 2022). The donor vector consisted in a CAG
707 promoter followed by the flipped ptxA coding sequence flanked by double inverted lox
708 sites (loxP and lox2272; Figure 2 Supp. 1C) and a bGHpA sequence. In order to
709 exclude the prokaryotic vector backbone, the donor vector was prepared as a minicircle
710 using the MC-Easy Minicircle Production kit (SystemBio, MN920A-1). Briefly, the donor
711 plasmid insert was cloned into a Minicircle Cloning Vector using PhiC31 integrase
712 before transformation into the ZYCY10P3S2T *E. coli* minicircle producer strain, which
713 after induction with arabinose, results in the generation of the donor minicircle. To
714 eliminate parental plasmid contamination, a restriction digest was performed, followed
715 by MC-safe DNase treatment. The minicircle DNA was then purified by phenol-
716 chloroform extraction and reconstituted in microinjection buffer (10 mM Tris; 0.1 mM
717 EDTA pH7.5). The *CAG-DIO-ptxA* strain was generated by pronuclear microinjection of
718 the Bxb1 Integration reagents directly into zygotes of the host strain. These reagents
719 included the Bxb1 mRNA (Trilink) at 100ng/µl, RNasin (Promega) at 0.2U/µl and the
720 donor minicircle DNA at 10ng/µl combined in microinjection buffer. To confirm
721 successful integration of the 3,212bp transgene, as well as identify random transgenics,
722 the initial screening was performed using a four-PCR strategy. The In/Out Left and
723 Right (IOL, IOR) PCRs, which bridge the recombined attachment sites, each contain
724 one primer specific to the *R26* locus and a second primer designed against the inserted
725 sequence. The Transgene (TG) PCR amplifies a non-genomic sequence in the insert,
726 and the Off-Target Integration (OTI) PCR was designed to detect non-recombined
727 minicircle integration, presumably outside of the *R26* locus.
728 IOL PCR (F1/R1), F1: GTCGCTCTGAGTTGTTATCAGT, R1:
729 GCCAAGTAGGAAAGTCCCATAA (720 bp, WT=no band). IOR PCR (F2/R2), F2:
730 GGTGATGCCGTTGTGATAGA, R2: TGTGGGAAGTCTTGTCCCTCCAAT (1,013 bp,
731 WT=no band). TG PCR (F2/R3) F2: 5'-GGTGATGCCGTTGTGATAGA, R3:
732 CCACTTCATCGGCTACATCTAC (214 bp, WT=no band). OTI PCR (F3/R1) F3:
733 GGGAGGATTGGGAAGACAATAG, R1: GCCAAGTAGGAAAGTCCCATAA (578 bp,

734 WT=no band). 33 mice were born following 6 transfers totaling 117 injected embryos
735 (28% survival), and 1/33 (3%) was identified as a founder and crossed to C57BL6/J to
736 generate N1 offspring. The In/Out PCR confirmed that a copy of the transgene was
737 inserted at the *R26* locus, but the OTI strategy also gave a product, even after breeding
738 for multiple generations. As breeding would have segregated a separate, random
739 integration of the transgene, we performed Nanopore-based Cas9-targeted sequencing
740 at the *R26* locus (Gilpatrick et al, 2020; Low et al, 2022). This revealed that, as seen in
741 some cases previously (Low et al, 2022), tandem insertions had occurred in this founder
742 Specifically, 3 consecutive copies of the *CAG-DIO-ptxA* transgene were inserted at the
743 *R26* locus in this strain. This did not impact specific Cre-based expression of ptxA
744 because phenotypes observed in this new strain were comparable to the previous *LSL-*
745 *myc:ptxA* strain (Figure 6 Supp.1 B-D).
746
747 Experimental animals in the study ranged in age between E17.5 and P29 as indicated in
748 each figure. Male and females were systematically included but sex was not tracked
749 except for Auditory Brainstem Recordings because there is no evidence that sex
750 influences HC orientation or hair bundle morphogenesis. Animals were maintained
751 under standard housing conditions (14h light / 10h dark cycle, ambient temperature and
752 normal humidity). All animal work was reviewed for compliance and approved by the
753 Animal Care and Use Committee of The Jackson Laboratory (Animal Use Summary
754 AUS #14012).
755
756 **Scanning Electron Microscopy (SEM)**
757 Temporal bones were isolated, punctured at the cochlear apex, and fixed by immersion
758 for at least one overnight at 4°C in 2.5% glutaraldehyde (Electron Microscopy Sciences;
759 16200) and 4% paraformaldehyde (Electron Microscopy Sciences; 15710) in 1mM
760 $MgCl_2$, 0.1M Sodium Cacodylate, 20mM $CaCl_2$. Samples were rinsed and decalcified
761 overnight in 4% EDTA. The auditory epithelium was then dissected into 3 pieces
762 (cochlear base, mid, and apex) before progressive dehydration in an ethanol series (30-
763 50-70-80-90-100%, at least 20 minutes per step) and chemical drying with
764 hexamethyldisilazane (HMDS; Electron Microscopy Sciences 50-243-18). Dry samples

765 were mounted on aluminum stubs using double-sided carbon tape and sputter-coated
766 with gold-palladium before imaging on a Hitachi 3000N VP electronic microscope at
767 20kV.
768
769 **Immunofluorescence and antibodies**
770 For embryonic and postnatal stages, temporal bones were either immediately dissected
771 to expose the sensory epithelium and fixed in paraformaldehyde (PFA 4%; Electron
772 Microscopy Sciences; 15710) for 1h at 4°C. After fixation, the tectorial membrane was
773 removed, and samples were permeabilized and blocked in PBS with 0.5% Triton-X100
774 and bovine serum albumin (1%) for at least at 1 hour at room temperature. For adult
775 stages, temporal bones were isolated and punctured at the cochlear apex to facilitate
776 access for the fixative. Samples were then immersion-fixed in PFA 4% for 1 hour at 4°C,
777 rinsed in PBS, and incubated overnight in 4% EDTA for decalcification. Cochleae were
778 next dissected in 3 pieces (cochlear base, mid, and apex), before permeabilization and
779 blocking as described for earlier stages. Primary and secondary antibodies were
780 incubated overnight at 4°C in PBS with 0.025% sodium azide. Fluorescent dye-
781 conjugated phalloidin was added to secondary antibodies. Samples were washed 3
782 times in PBS + 0.05% Triton-X100 after each antibody incubation and post-fixed in PFA
783 4% for at least 1 hour at room temperature. Samples were then mounted flat on
784 microscopy slides (Denville M102) using Mowiol as mounting medium
785 (Calbiochem/MilliporeSigma 4759041), either directly under a 18x18mm #1.5
786 coverglass (VWR 48366-045) (postnatal cochleae) or using one layer of office tape as a
787 spacer (adult cochleae). Mowiol (10% w/v) was prepared in 25%(w/v) glycerol and 0.1M
788 Tris-Cl pH8.5. Primary antibodies used were:
789
790 Rabbit anti-GNAI2, pt"GNAI2" (Proteintech, 11136-1-AP); the antigen is the full human
791 GNAI2 protein, and GNAI1 is a closer paralog to GNAI2 compared to GNAI3.
792 Rabbit anti-GNAI3, scbt"GNAI3" (Santa Cruz Biotechnology, sc-262); the C-terminal rat
793 antigen was not disclosed but the company indicated that this product detects
794 preferentially GNAI3>GNAI1>GNAI2.
795 Rabbit anti-GNAO (Proteintech, 12635-1-AP)

796 Mouse anti-acetylated alpha tubulin (Santa Cruz Biotechnology scbt-23950)
797 Rabbit anti-GPSM2 (Sigma, A41537)
798 Goat anti-GPSM2 (Thermofisher, PA5-18646)
799 Rabbit anti-Pericentrin/PCNT (Biolegend/Covance, PRB-432C)
800 Rat anti-ZO1 (Developmental Studies Hybridoma Bank, R26.4C)
801
802 Secondary antibodies from ThermoFisher Scientific were raised in donkey and
803 conjugated to Alexa Fluor (AF) 488, 555, or 647 (donkey anti-rabbit AF555 (A-31572),
804 AF647 (A-31573), donkey anti-mouse AF647 (A-31571), donkey anti-rat AF488 (A-
805 21208), donkey anti-goat AF555 (A-21432), AF647 (A-21447)). Fluorescent conjugated
806 phalloidins used to reveal F-actin were from ThermoFisher Scientific: AF488 (A12379);
807 AF555 (A34005) and Sigma-Aldrich: FITC (P5282).
808
809 **Sample cohorts, image acquisition and analysis**
810 All quantifications included at least three animals per genotype. All graphs or their
811 legends indicate the animal cohort size (N) as well as the number of HC or stereocilia
812 (n) analyzed. Further details can be found in a single Supplementary Source Data file
813 where tabs are referencing figure panels in order. When an experimental outcome was
814 not quantified, at least 3 mutant and 3 control littermates encompassing two or more
815 litters were analyzed, and figure panels illustrate a representative outcome observed in
816 all samples of the same genotype.
817
818 Confocal images were captured with a LSM800 line scanning confocal microscope, a
819 63x NA1.4 oil objective, the Airyscan detector in confocal mode (except in Figure 5
820 Supp.1 D, E where the Airyscan detector was used in Airyscan mode) and the Zen 2.3
821 or Zen 2.6 software (Carl Zeiss AG). Raw Airyscan images in Figure 5 Supp.1 D, E
822 were processed in Zen 2.6 selecting for automatic strength. Unless stated otherwise in
823 the legends, images show a single optical z plane. To quantify HCs eccentricity (Figure
824 7), images were captured with a Leica DM5500B widefield microscope, a 63x oil
825 objective, a Hamamatsu ORCA-Flash4.0 sCMOS camera and the Leica Application
826 Suite (LasX) software (Leica Microsystems). All images in the same experiment were

827 acquired using the same laser intensity and gain, and were then processed in Adobe
828 Photoshop (CC2020) where the same image treatment was applied across conditions.
829
830 To measure stereocilia length and width in IHCs (Figure 2C-D), SEM samples were
831 imaged laterally with a 10,000x magnification and an appropriate tilt (from 0 to 30°) to
832 bring stereocilia parallel to the imaging plane and minimize parallax. To quantify the
833 number of rows in adult IHCs and the number of stereocilia in their first row (Figure 2E,
834 F), SEM samples were imaged medially with a 5,000x magnification. To measure the
835 length of OHC hair bundle wings (Figure 2G, Figure 2 Supp. 1G), OHCs were imaged
836 from the top at 5,000x. Stereocilia width was measure at half-length and all
837 measurements were done with the straight-line tool in Fiji.
838
839 To quantify GNAI signal intensity in *Gnai1*^{neo}*; Gnai3*^{neo} mutants (Figure 5C, Figure 5
840 Supp. 1A), Z-stack series were acquired at the one-turn cochlear position. A single Z
841 slice was chosen at the bare zone level, another one at the stereocilia tip level, each
842 based on strongest signal in that compartment. The vertex of the V-shaped hair bundle
843 was used to divide the HC apical surface in two equal halves. In each half (left and
844 right), regions of interest (ROIs) were drawn using the polygon selection tool in Fiji to
845 encompass all signals in that apical compartment, and mean gray values were
846 measured. For each image, background signal was measured and averaged, and
847 subtracted from all measurements in the same image.
848
849 To quantify surface area of the bare zone or total surface area in half-OHC as well as
850 the length of half hair bundles (Figure 5G, Figure 5 Supp. 1C; Figure 6D, H), Z-stack
851 series were acquired at the cochlear base and a single Z slice was selected at apical
852 junction level using ZO1 (Figure 5G, Figure 5 Supp. 1C) or F-actin (Figure 6D, H) as
853 reference. To measure total apical surface area and bundle length in half-OHCs, the
854 pericentrin-stained basal body was used to divide the apical surface in two halves
855 (Figure 5G, Figure 5 Supp. 1C). The ZO1-positive cell outline along with the dividing line
856 at the basal body level were used as reference to measure surface area with the
857 polygon selection tool in Fiji. To quantify the bare zone surface area (Figure 6D, H), a

858 ROI was drawn around the total apical surface lacking phalloidin (F-actin) signals. The
859 length of the F-actin stained hair bundle was measured using the straight-line tool in Fiji.
860
861 To determine HC eccentricity (Figure 7), the geometrical center of the HC apical surface
862 was determined as the intersection of two orthogonal lines representing the maximal
863 diameter of the cell along the cochlear longitudinal and radial axes. A vector (BB) was
864 drawn from the center to the pericentrin-labeled basal body, and eccentricity was
865 calculated as the ratio of BB length over the cell radius (r) along the same trajectory
866 using F-actin-labeled apical junction as landmark (see Figure 7). To determine cell
867 orientation (Figure 8 and Figure 8 Supp. 1), the angle (α) separating the longitudinal
868 axis of the organ of Corti from the BB vector was measured with the angle tool in Fiji
869 (see Figure 8). Both right and left cochleae were used and angles were measured so
870 that 0° pointed toward the cochlear base and 90° towards the cochlear periphery
871 (lateral). Eccentricity and angles were measured at the positions indicated (base ~20%,
872 mid ~50%, apex ~80% of the cochlear length starting from the base).
873
874 **Auditory Brainstem Response (ABR) tests**
875 All tests were performed in a sound-attenuating chamber, and body temperature of the
876 anesthetized animals was maintained at 37°C using a heating pad (FHC Inc.). Animals
877 from all strains except *Atoh1-Cre; Gnao*^{flox} (Figure 3 Supp. 1B, see below) were
878 anesthetized with a mix of ketamine and xylazine (1 mg and 0.8 mg per 10g of body
879 weight, respectively) and tested using the RZ6 Multi-I/O Processor System coupled to
880 the RA4PA 4-channel Medusa Amplifier (Tucker-Davis Technologies). ABRs were
881 recorded after binaural stimulation in an open field by tone bursts at 8, 16, 32, and 40
882 kHz generated at 21 stimuli/second, and a waveform for each frequency/dB level was
883 produced by averaging the responses from 512 stimuli. Subdermal needles were used
884 as electrodes, the active electrode inserted at the cranial vertex, the reference electrode
885 under the left ear and the ground electrode at the right thigh.
886 *Atoh1-Cre; Gnao1*^{flox} animals (Figure 3 Supp. 1B) were anesthetized with
887 tribromoethanol (2.5mg per 10g of body weight) and tested with the Smart EP evoked
888 potential system from Intelligent Hearing Systems (IHS). ABR were recorded after

single ear stimulation (right ear), using ear tubes speakers (ER3C insert earphones, IHS) delivering tone bursts at 8, 16, and 32 kHz generated at 40 stimuli/second. Electrodes were positioned as previously described except for the ground electrode that was placed at the base of the tail. ABR thresholds were obtained for each frequency by reducing the sound pressure level (SPL) by 5 decibels (dB) between 90 and 20 dB to identify the lowest level at which an ABR waveform could be recognized. We compared waveforms by simultaneously displaying 3 or more dB levels on screen at the same time.

Statistical Analyses

All data were plotted in Prism 9 (GraphPad), except for circular diagrams of HC orientation (Figure 8; Figure 8 Supp. 1) that were generated with R (4.2.2) and Rstudio (2022.12.0+353).

All data except for angles in circular diagrams (Figure 8 and Figure 8 Supp. 1) were plotted individually. Distribution was framed with 25-75% whisker boxes where exterior lines show the minimum and maximum, the middle line represents the median, and + represents the mean. Potential differences in data distribution between genotypes were tested for significance using Mann-Whitney U test (non-parametric unpaired test), except for ABR thresholds (Figure 3 and Figure 3 Supp. 1) where a 2-way ANOVA with Sidak's multiple comparison post-hoc test was used. OHC half-bundle lengths (Figure 2G, Figure 2 Supp. 1G) were plotted as paired left and right values in the same HC and a potential difference in data variance between genotypes was tested using a F-test. GNAI signal intensity at the OHC bare zone and stereocilia tips (Figure 5C, Figure 5 Supp. 1A) as well as OHC surface area and half-bundle length (Figure 5G, Figure 5 Supp. 1C) were plotted and a simple linear regression curve was calculated and drawn for each pair of datasets. A correlation between variables was addressed with Pearson's correlation test. Exact p-values were indicated on each graph when non-significant ($p>0.05$) and otherwise summarized a follows: $p<0.0001$ ****, $p<0.001$ ***, $p<0.01$**, $p<0.05$. Details of statistical results for all figures can be found in the Supplementary Data file.

Angle frequency distribution (Figure 8 and Figure 8 Supp. 1) was plotted in circular diagrams using the R package dyplr and the coord_polar function of the ggplot2 package to organize data and produce the graphs, respectively. The angle formed by the red line indicates the circular mean and the length of the arc at the end of the red line indicates the mean circular deviation. Both values were obtained using the colstats function in the R circular package. All scripts used in this work will be posted on github.

ACKNOWLEDGMENTS

We are grateful to Elli Hartig for reading and commenting on the manuscript. We thank Simon Lesbirel for nanopore-based Cas9-targeted sequencing of the *DIO-ptxA* strain. We are grateful to The Jackson Laboratory Genome Engineering Technology and Reproductive Science services for their help with generating the *Gnai2*^{del} and *Gnai3*^{flox} strains, and cryorecovering the *Gnai1*^{neo}*; Gnai3*^{neo} and *Gnao1*^{neo} strains, respectively. A.J. was supported by a postdoctoral fellowship from Fondation Pour l'Audition (2018-2020; FPA RD-2018-3). This work was supported by the National Institute on Deafness and Other Communication Disorders grants R01DC015242 and R01DC018304 (to B.T.).

AUTHOR CONTRIBUTION

B.T. conceived the study and designed most experiments. A.J and A.L.T designed, performed and analyzed experiments. M.D. provided technical help with mouse colony maintenance, sample processing and genotyping. B. K. wrote the R script to generate the circular histograms. B.E.L and M.V.W. helped generate the *DIO-ptxA* strain using BxB1 recombination technology. B.T supervised the work. B.T. and A.J. wrote the manuscript. B.T. secured funding.

COMPETETING INTERESTS

The authors declare no competing interest.

DATA AVAILABILITY

The data in all graphical representations are included in a single Source Data file. Original material used for quantifications and to build figures will be deposited in a publicly accessible repository.

959 **REFERENCES**

960

961 Akturk, A., Day, M. & Tarchini, B. (2022) RGS12 polarizes the GPSM2-GNAI complex to
962 organize and elongate stereocilia in sensory hair cells. *Sci Adv*, 8(42), eabq2826.

963 Beer-Hammer, S., Lee, S. C., Mauriac, S. A., Leiss, V., Groh, I. A. M., Novakovic, A.,
964 Piekorz, R. P., Bucher, K., Chen, C., Ni, K., Singer, W., Harasztosi, C., Schimmang, T.,
965 Zimmermann, U., Pfeffer, K., Birnbaumer, L., Forge, A., Montcouquiol, M., Knipper, M.,
966 Nurnberg, B. & Ruttiger, L. (2018) Galphai Proteins are Indispensable for Hearing. *Cell*
967 *Physiol Biochem*, 47(4), 1509-1532.

968 Bhonker, Y., Abu-Rayyan, A., Ushakov, K., Amir-Zilberstein, L., Shivatzki, S., Yizhar-
969 Barnea, O., Elkan-Miller, T., Tayeb-Fligelman, E., Kim, S. M., Landau, M., Kanaan, M.,
970 Chen, P., Matsuzaki, F., Sprinzak, D. & Avraham, K. B. (2016) The GPSM2/LGN
971 GoLoco motifs are essential for hearing. *Mamm Genome*, 27(1-2), 29-46.

972 Deans, M. R. (2013) A balance of form and function: planar polarity and development of
973 the vestibular maculae. *Semin Cell Dev Biol*, 24(5), 490-8.

974 Denman-Johnson, K. & Forge, A. (1999) Establishment of hair bundle polarity and
975 orientation in the developing vestibular system of the mouse. *J Neurocytol*, 28(10-11),
976 821-35.

977 Doherty, D., Chudley, A. E., Coghlan, G., Ishak, G. E., Innes, A. M., Lemire, E. G.,
978 Rogers, R. C., Mhanni, A. A., Phelps, I. G., Jones, S. J., Zhan, S. H., Fejes, A. P.,
979 Shahin, H., Kanaan, M., Akay, H., Tekin, M., Consortium, F. C., Triggs-Raine, B. &
980 Zelinski, T. (2012) GPSM2 mutations cause the brain malformations and hearing loss in
981 Chudley-McCullough syndrome. *Am J Hum Genet*, 90(6), 1088-93.

982 Du, Q., Stukenberg, P. T. & Macara, I. G. (2001) A mammalian Partner of inscuteable
983 binds NuMA and regulates mitotic spindle organization. *Nat Cell Biol*, 3(12), 1069-75.

984 Etournay, R., Lepelletier, L., Boutet de Monvel, J., Michel, V., Cayet, N., Leibovici, M.,
985 Weil, D., Foucher, I., Hardelin, J. P. & Petit, C. (2010) Cochlear outer hair cells undergo
986 an apical circumference remodeling constrained by the hair bundle shape.
987 *Development*, 137(8), 1373-83.

988 Ezan, J., Lasvaux, L., Gezer, A., Novakovic, A., May-Simera, H., Belotti, E., Lhoumeau,
989 A. C., Birnbaumer, L., Beer-Hammer, S., Borg, J. P., Le Bivic, A., Nurnberg, B., Sans,
990 N. & Montcouquiol, M. (2013) Primary cilium migration depends on G-protein signalling
991 control of subapical cytoskeleton. *Nat Cell Biol*, 15(9), 1107-15.

992 Gilpatrick, T., Lee, I., Graham, J. E., Raimondeau, E., Bowen, R., Heron, A., Downs, B.,
993 Sukumar, S., Sedlazeck, F. J. & Timp, W. (2020) Targeted nanopore sequencing with
994 Cas9-guided adapter ligation. *Nat Biotechnol*, 38(4), 433-438.

995 Gohla, A., Klement, K., Piekorz, R. P., Pexa, K., vom Dahl, S., Spicher, K., Dreval, V.,
996 Häussinger, D., Birnbaumer, L. & Nürnberg, B. (2007) An obligatory requirement for the
997 heterotrimeric G protein Gi3 in the antiautophagic action of insulin in the liver. *Proc Natl*
998 *Acad Sci U S A*, 104(8), 3003-8.

999 Greene, D., Genomics England Research, C., Pirri, D., Frudd, K., Sackey, E., Al-Owain,
1000 M., Giese, A. P. J., Ramzan, K., Riaz, S., Yamanaka, I., Boeckx, N., Thys, C., Gelb, B.
1001 D., Brennan, P., Hartill, V., Harvengt, J., Kosho, T., Mansour, S., Masuno, M., Ohata, T.,
1002 Stewart, H., Taibah, K., Turner, C. L. S., Imtiaz, F., Riazuddin, S., Morisaki, T.,
1003 Ostergaard, P., Loeys, B. L., Morisaki, H., Ahmed, Z. M., Birdsey, G. M., Freson, K.,
1004 Mumford, A. & Turro, E. (2023) Genetic association analysis of 77,539 genomes reveals
1005 rare disease etiologies. *Nat Med*.

1006 Hebert, J. M. & McConnell, S. K. (2000) Targeting of cre to the Foxg1 (BF-1) locus
1007 mediates loxP recombination in the telencephalon and other developing head
1008 structures. *Dev Biol*, 222(2), 296-306.

1009 Jarysta, A. & Tarchini, B. (2021) Multiple PDZ domain protein maintains patterning of
1010 the apical cytoskeleton in sensory hair cells. *Development*, 148(14).

1011 Jiang, M., Gold, M. S., Boulay, G., Spicher, K., Peyton, M., Brabet, P., Srinivasan, Y.,
1012 Rudolph, U., Ellison, G. & Birnbaumer, L. (1998) Multiple neurological abnormalities in
1013 mice deficient in the G protein Go. *Proc Natl Acad Sci U S A*, 95(6), 3269-74.

1014 Jiang, M., Spicher, K., Boulay, G., Martin-Requero, A., Dye, C. A., Rudolph, U. &
1015 Birnbaumer, L. (2002) Mouse gene knockout and knockin strategies in application to
1016 alpha subunits of Gi/Go family of G proteins. *Methods Enzymol*, 344, 277-98.

1017 Jiang, T., Kindt, K. & Wu, D. K. (2017) Transcription factor Emx2 controls stereociliary
1018 bundle orientation of sensory hair cells. *Elife*, 6.

1019 Jones, C., Roper, V. C., Foucher, I., Qian, D., Banizs, B., Petit, C., Yoder, B. K. & Chen,
1020 P. (2008) Ciliary proteins link basal body polarization to planar cell polarity regulation.
1021 *Nat Genet*, 40(1), 69-77.

1022 Kindt, K. S., Akturk, A., Jarysta, A., Day, M., Beirl, A., Flonard, M. & Tarchini, B. (2021)
1023 EMX2-GPR156-Galphai reverses hair cell orientation in mechanosensory epithelia. *Nat*
1024 *Commun*, 12(1), 2861.

1025 Locht, C., Coutte, L. & Mielcarek, N. (2011) The ins and outs of pertussis toxin. *FEBS J*,
1026 278(23), 4668-82.

1027 Low, B. E., Hosur, V., Lesbirel, S. & Wiles, M. V. (2022) Efficient targeted transgenesis
1028 of large donor DNA into multiple mouse genetic backgrounds using bacteriophage Bxb1
1029 integrase. *Sci Rep*, 12(1), 5424.

1030 Matei, V., Pauley, S., Kaing, S., Rowitch, D., Beisel, K. W., Morris, K., Feng, F., Jones,
1031 K., Lee, J. & Fritzsch, B. (2005) Smaller inner ear sensory epithelia in Neurog 1 null
1032 mice are related to earlier hair cell cycle exit. *Dev Dyn*, 234(3), 633-50.

1033 Mauriac, S. A., Hien, Y. E., Bird, J. E., Carvalho, S. D., Peyroutou, R., Lee, S. C.,
1034 Moreau, M. M., Blanc, J. M., Geyser, A., Medina, C., Thoumine, O., Beer-Hammer, S.,
1035 Friedman, T. B., Ruttiger, L., Forge, A., Nurnberg, B., Sans, N. & Montcouquiol, M.
1036 (2017) Defective Gpsm2/Galphai3 signalling disrupts stereocilia development and
1037 growth cone actin dynamics in Chudley-McCullough syndrome. *Nat Commun*, 8, 14907.

1038 May-Simera, H. L., Petralia, R. S., Montcouquiol, M., Wang, Y. X., Szarama, K. B., Liu,
1039 Y., Lin, W., Deans, M. R., Pazour, G. J. & Kelley, M. W. (2015) Ciliary proteins Bbs8
1040 and Ift20 promote planar cell polarity in the cochlea. *Development*, 142(3), 555-66.

1041 Mbiene, J. P. & Sans, A. (1986) Differentiation and maturation of the sensory hair
1042 bundles in the fetal and postnatal vestibular receptors of the mouse: a scanning electron
1043 microscopy study. *J Comp Neurol*, 254(2), 271-8.

1044 Montcouquiol, M. & Kelley, M. W. (2019) Development and Patterning of the Cochlea:
1045 From Convergent Extension to Planar Polarity. *Cold Spring Harb Perspect Med*.

1046 Plummer, N. W., Spicher, K., Malphurs, J., Akiyama, H., Abramowitz, J., Nürnberg, B. &
1047 Birnbaumer, L. (2012) Development of the mammalian axial skeleton requires signaling
1048 through the Gα(i) subfamily of heterotrimeric G proteins. *Proc Natl Acad Sci U S A*,
1049 109(52), 21366-71.

1050 Qin, W., Dion, S. L., Kutny, P. M., Zhang, Y., Cheng, A. W., Jillette, N. L., Malhotra, A.,
1051 Geurts, A. M., Chen, Y. G. & Wang, H. (2015) Efficient CRISPR/Cas9-Mediated
1052 Genome Editing in Mice by Zygote Electroporation of Nuclease. *Genetics*, 200(2), 423-
1053 30.

1054 Regard, J. B., Kataoka, H., Cano, D. A., Camerer, E., Yin, L., Zheng, Y. W., Scanlan, T.
1055 S., Hebrok, M. & Coughlin, S. R. (2007) Probing cell type-specific functions of Gi in vivo
1056 identifies GPCR regulators of insulin secretion. *J Clin Invest*, 117(12), 4034-43.

1057 Schaefer, M., Petronczki, M., Dorner, D., Forte, M. & Knoblich, J. A. (2001)
1058 Heterotrimeric G proteins direct two modes of asymmetric cell division in the Drosophila
1059 nervous system. *Cell*, 107(2), 183-94.

1060 Schaefer, M., Shevchenko, A., Shevchenko, A. & Knoblich, J. A. (2000) A protein
1061 complex containing Inscuteable and the Galpha-binding protein Pins orients asymmetric
1062 cell divisions in Drosophila. *Curr Biol*, 10(7), 353-62.

1063 Schnutgen, F., Doerflinger, N., Calleja, C., Wendling, O., Chambon, P. & Ghyselinck, N.
1064 B. (2003) A directional strategy for monitoring Cre-mediated recombination at the
1065 cellular level in the mouse. *Nat Biotechnol*, 21(5), 562-5.

1066 Siletti, K., Tarchini, B. & Hudspeth, A. J. (2017) Daple coordinates organ-wide and cell-
1067 intrinsic polarity to pattern inner-ear hair bundles. *Proc Natl Acad Sci U S A*, 114(52),
1068 E11170-E11179.

1069 Sipe, C. W. & Lu, X. (2011) Kif3a regulates planar polarization of auditory hair cells
1070 through both ciliary and non-ciliary mechanisms. *Development*, 138(16), 3441-9.

1071 Tadenev, A. L. D., Akturk, A., Devanney, N., Mathur, P. D., Clark, A. M., Yang, J. &
1072 Tarchini, B. (2019) GPSM2-GNAI Specifies the Tallest Stereocilia and Defines Hair
1073 Bundle Row Identity. *Curr Biol*, 29(6), 921-934 e4.

1074 Tarchini, B. (2021) A Reversal in Hair Cell Orientation Organizes Both the Auditory and
1075 Vestibular Organs. *Front Neurosci*, 15, 695914.

1076 Tarchini, B., Jolicoeur, C. & Cayouette, M. (2013) A molecular blueprint at the apical
1077 surface establishes planar asymmetry in cochlear hair cells. *Dev Cell*, 27(1), 88-102.

1078 Tarchini, B. & Lu, X. (2019) New insights into regulation and function of planar polarity
1079 in the inner ear. *Neurosci Lett*, 709, 134373.

1080 Tarchini, B., Tadenev, A. L., Devanney, N. & Cayouette, M. (2016) A link between
1081 planar polarity and staircase-like bundle architecture in hair cells. *Development*,
1082 143(21), 3926-3932.

1083 Tilney, L. G., Tilney, M. S. & DeRosier, D. J. (1992) Actin filaments, stereocilia, and hair
1084 cells: how cells count and measure. *Annu Rev Cell Biol*, 8, 257-74.

1085 Tona, Y. & Wu, D. K. (2020) Live imaging of hair bundle polarity acquisition
1086 demonstrates a critical timeline for transcription factor Emx2. *Elife*, 9.

1087 Walsh, T., Shahin, H., Elkan-Miller, T., Lee, M. K., Thornton, A. M., Roeb, W., Abu
1088 Rayyan, A., Loulus, S., Avraham, K. B., King, M. C. & Kanaan, M. (2010) Whole exome
1089 sequencing and homozygosity mapping identify mutation in the cell polarity protein
1090 GPSM2 as the cause of nonsyndromic hearing loss DFNB82. *Am J Hum Genet*, 87(1),
1091 90-4.

1092 Webb, S. W., Grillet, N., Andrade, L. R., Xiong, W., Swarthout, L., Della Santina, C. C.,
1093 Kachar, B. & Muller, U. (2011) Regulation of PCDH15 function in mechanosensory hair
1094 cells by alternative splicing of the cytoplasmic domain. *Development*, 138(8), 1607-17.

1095 Woodard, G. E., Huang, N. N., Cho, H., Miki, T., Tall, G. G. & Kehrl, J. H. (2010) Ric-8A
1096 and Gi alpha recruit LGN, NuMA, and dynein to the cell cortex to help orient the mitotic
1097 spindle. *Mol Cell Biol*, 30(14), 3519-30.

1098

1099

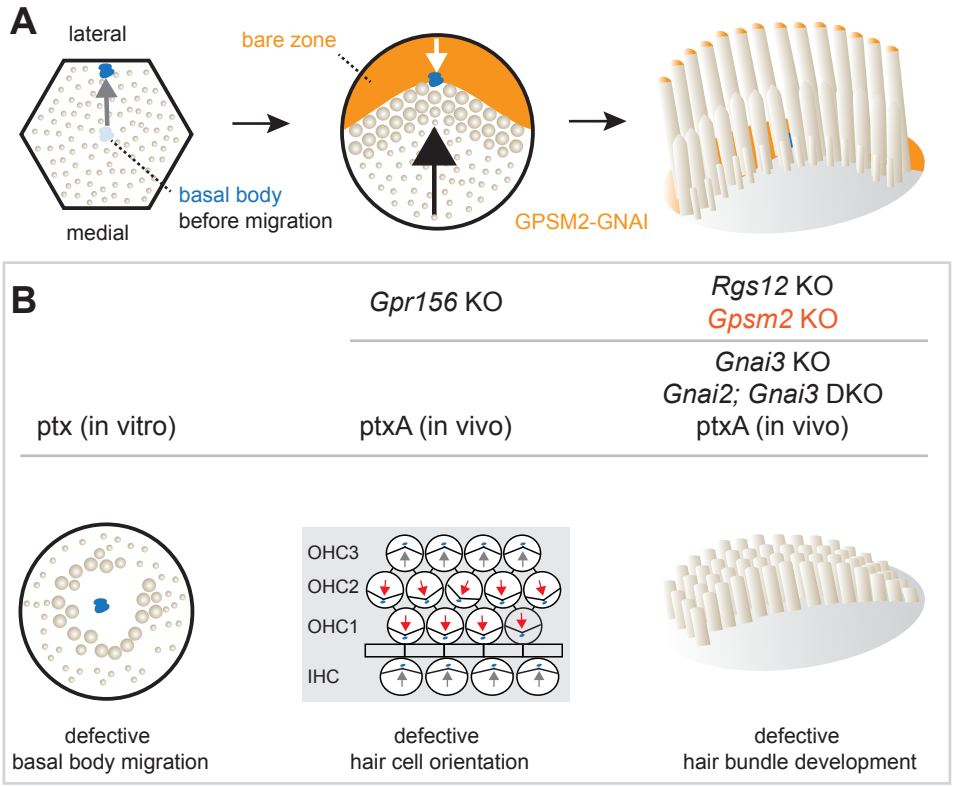

Figure 1. Summary of GNAI-related functions proposed previously. A) Apical HC differentiation from symmetry breaking to hair bundle development. The distribution of the GPSM2-GNAI complex at the bare zone and at stereocilia tips is indicated in orange. **B)** Defects observed with pertussis toxin (ptx) or when inactivating GNAI proteins. Defective off-center migration of the basal body and inverted OHC1-2s were only observed with ptx, respectively in cochlear explants (in vitro) and by expressing the ptx catalytic subunit (ptxA) in vivo. Mouse knock-out (KO)s of *Gnai* genes were to date only reported to affect hair bundle morphogenesis. Known GNAI regulators that produce similar defects when inactivated are indicated on top for each type of defect. DKO, double KO.

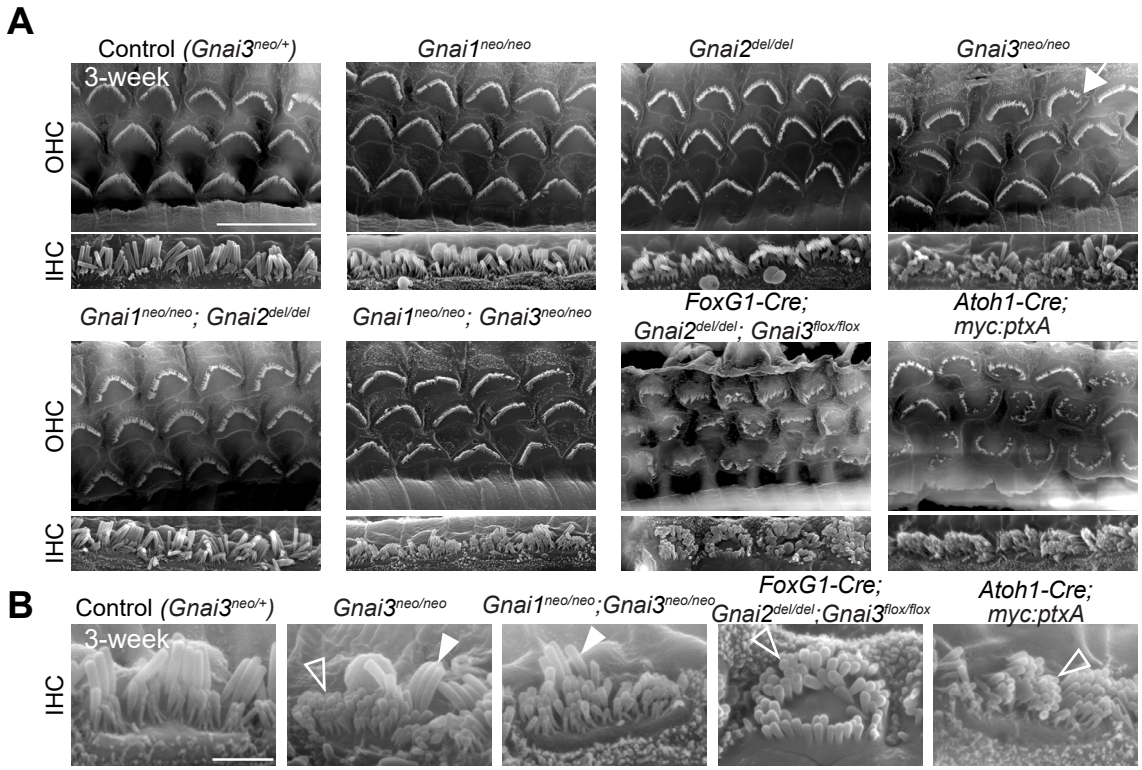
A
Control (Gnai3neo/+)
3-week
Gnai1neo/neo
Gnai2del/del
Gnai3neo/neo
OHC
IHC
Gnai1neo/neo; Gnai2del/del
Gnai1neo/neo; Gnai3neo/neo
FoxG1-Cre; Gnai2del/del; Gnai3flox/flox
Atoh1-Cre; myc:ptxA
B
Control (Gnai3neo/+)
3-week
Gnai3neo/neo
Gnai1neo/neo;Gnai3neo/neo
FoxG1-Cre; Gnai2del/del;Gnai3flox/flox
Atoh1-Cre; myc:ptxA
IHC

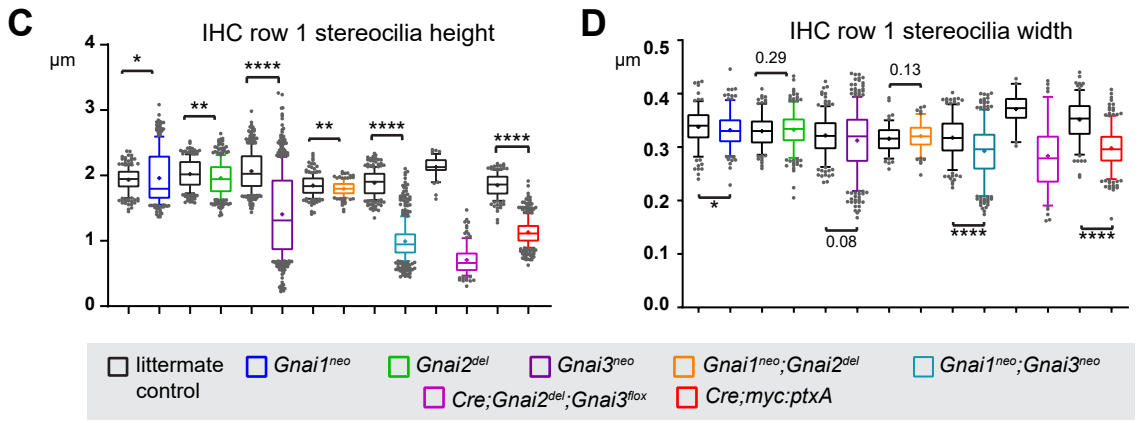
C
IHC row 1 stereocilia height
µm
D
IHC row 1 stereocilia width
µm
0.29
0.13
0.08
littermate control
Gnai1neo
Gnai2del
Gnai3neo
Gnai1neo;Gnai2del
Gnai1neo;Gnai3neo
Cre;Gnai2del;Gnai3flox
Cre;myc:ptxA

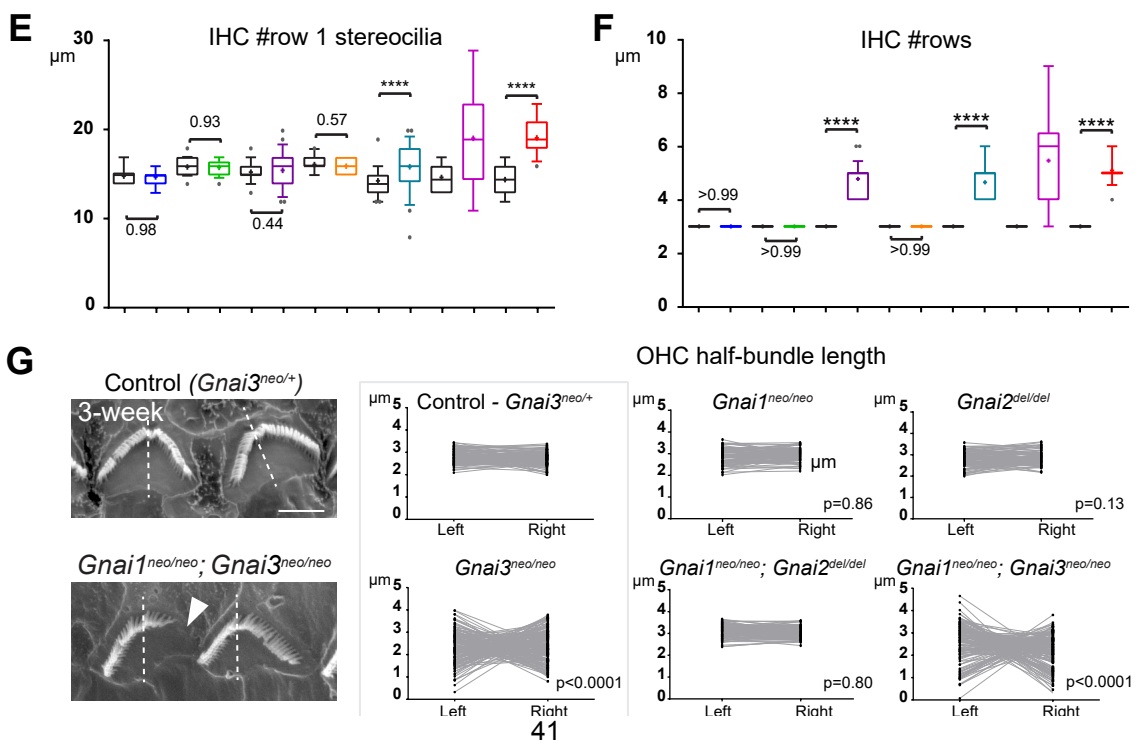
E
IHC #row 1 stereocilia
µm
0.98
0.93
0.44
0.57
F
IHC #rows
µm
>0.99
>0.99
>0.99
G
Control (Gnai3neo/+)
3-week
Gnai1neo/neo; Gnai3neo/neo
OHC half-bundle length
Control - Gnai3neo/+
Gnai1neo/neo
Gnai2del/del
Gnai3neo/neo
Gnai1neo/neo; Gnai2del/del
Gnai1neo/neo; Gnai3neo/neo
µm
Left
Right
p=0.86
p=0.13
p<0.0001
p=0.80
p<0.0001

Figure 2. Individual GNAI proteins make different contributions to hair bundle development. A-B) SEM images of representative OHCs (A) and IHCs (B) in 3-week old animals at the cochlear first turn. *Gnai1*^{neo}, *Gnai2*^{del}, and *Gnai1*^{neo}*; Gnai2*^{del} mutants show apparently normal hair bundle morphology in both HC types. In contrast, *Gnai3*^{neo} and *Gnai1*^{neo}*; Gnai3*^{neo} mutants show numerous defects in both HC types, including truncated hair bundles in OHCs (arrow), as well as supernumerary rows of stunted (hollow arrowheads) or longer stereocilia of variable height (full arrowheads) in IHCs. In addition, in *FoxG1-Cre; Gnai2*^{del}*; Gnai3*^{flox} and *Atoh1-Cre; LSL-myc:ptxA* mutants, OHC1-2s are severely misoriented. **C-F)** Quantification of various hair bundle features in 3-week old IHCs at the cochlear first turn. Each mutant strain is compared to littermate controls (in black; exact genotypes detailed in Source Data file). At least 3 animals, 17 IHCs and 108 stereocilia are represented per condition, except for *FoxG1-Cre; Gnai2*^{del}*; Gnai3*^{flox} where we could only obtain a single animal due to postnatal lethality. Mann-Whitney U test; $p<0.0001$ ****, $p<0.001$ ***, $p<0.01$ **, $p<0.05$ *; non-significant p-values are indicated. Detailed cohort sizes and statistics can be found in the Source Data file. **G)** SEM images of representative OHCs showing a truncated hair bundle (arrowhead). Lengths for the left and right wing of the hair bundle were measured and plotted as paired values for the same OHC. A littermate control graph is only shown for *Gnai3*^{neo} mutants (*Gnai3*$^{neo/+}$ littermate controls). Littermate control graphs for the other mutants can be found in Fig. 2 Supp. 1G. p-values are for a F-test of variance of pooled left and right wing lengths compared to littermate controls. At least 3 animals and 88 OHCs are represented per genotype. Only *Gnai3*^{neo} and *Gnai1*^{neo}; *Gnai3*^{neo} mutants show truncated hair bundles and a significant p value ($p<0.05$). Scale bars are 10μm (A) and 2μm (B, G).

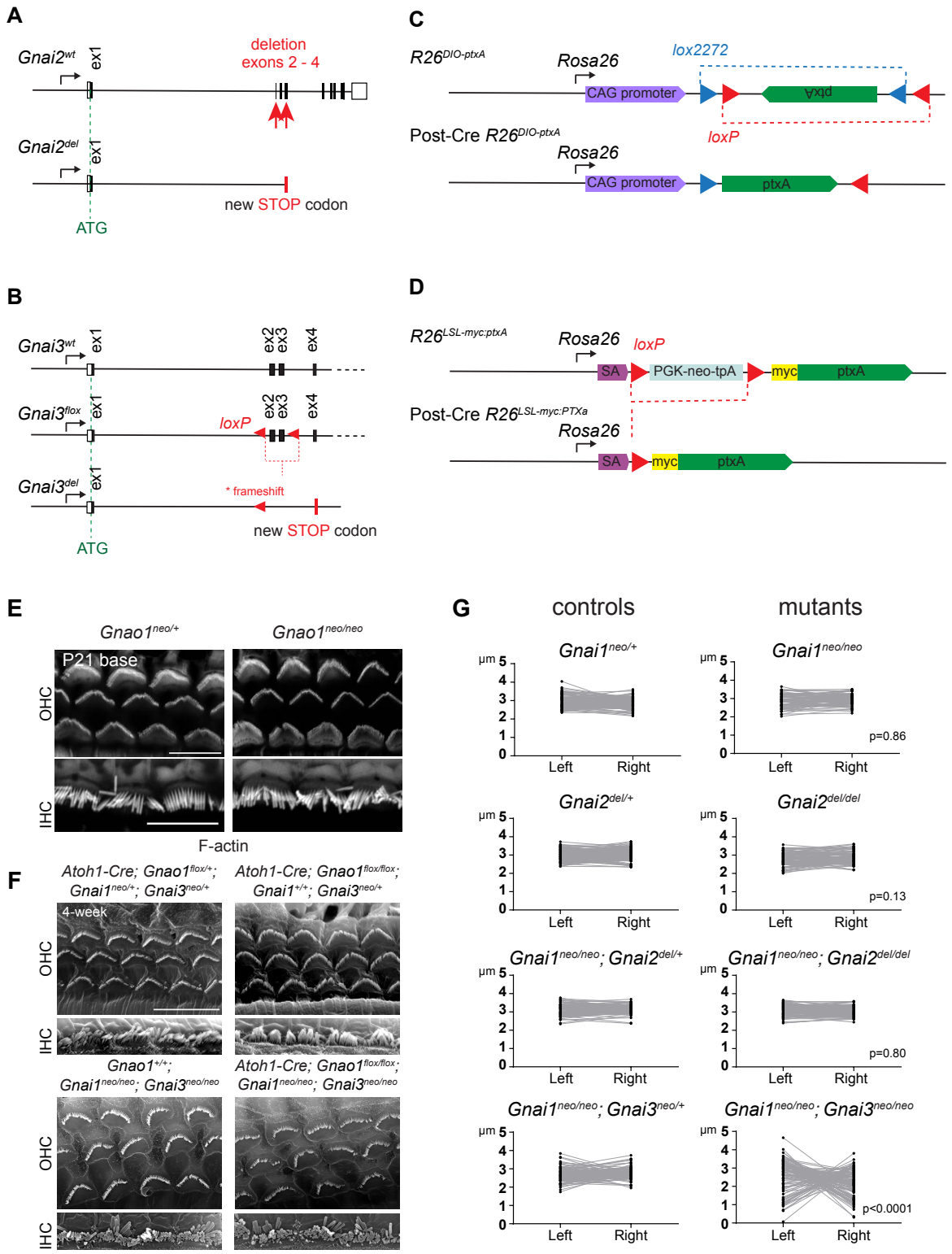

Figure 2 Supplement 1. A-D) New mouse strains generated in this study are *Gnai2*^{del} (A), *Gnai3*^{flox} (B) and *R26*$^{DIO\text{-}ptxA}$ (C; see Methods for details). *R26*$^{LSL\text{-}myc:ptxA}$ was published previously and is illustrated for comparison as it is used in the study as well (D). **E-F)** Loss of GNAO has no obvious impact on apical HC morphology or HC orientation. Representative confocal images of phalloidin-stained *Gnao1* constitutive mutants at P21 (E; *Gnao1*^{neo}) and scanning electron microscopy images of conditional *Gnao1* inactivation in the *Gnai1; Gnai3* double mutant background (F; *Gnao1*^{flox}). In F, top panels

compare control (left) and conditional *Gnao1* inactivation (right) when GNAI1 and GNAI3 functions are preserved. Bottom panels compare control (left) and conditional *Gnao1* inactivation (right) when GNAI1 and GNAI3 are inactivated. Note how HC-specific inactivation of GNAO using the *Atoh1-Cre* driver does not obviously enhance defects observed in *Gnai1; Gnai3* double mutants (F, bottom). **G)** Graphs showing the length of the left and right wing of 3 week-old OHC hair bundles paired by cell. Graphs for control littermates that were omitted in Fig. 2G are added here (left) next to repeated mutant graphs (right). p-values are for a F-test of variance of pooled left and right wing lengths compared to littermate controls. At least 3 animals and 88 OHCs are represented per genotype. Only *Gnai3*^{neo} (Fig. 2G) and *Gnai1*^{neo}; *Gnai3*^{neo} mutants show truncated hair bundles and a significant p value ($p<0.05$).

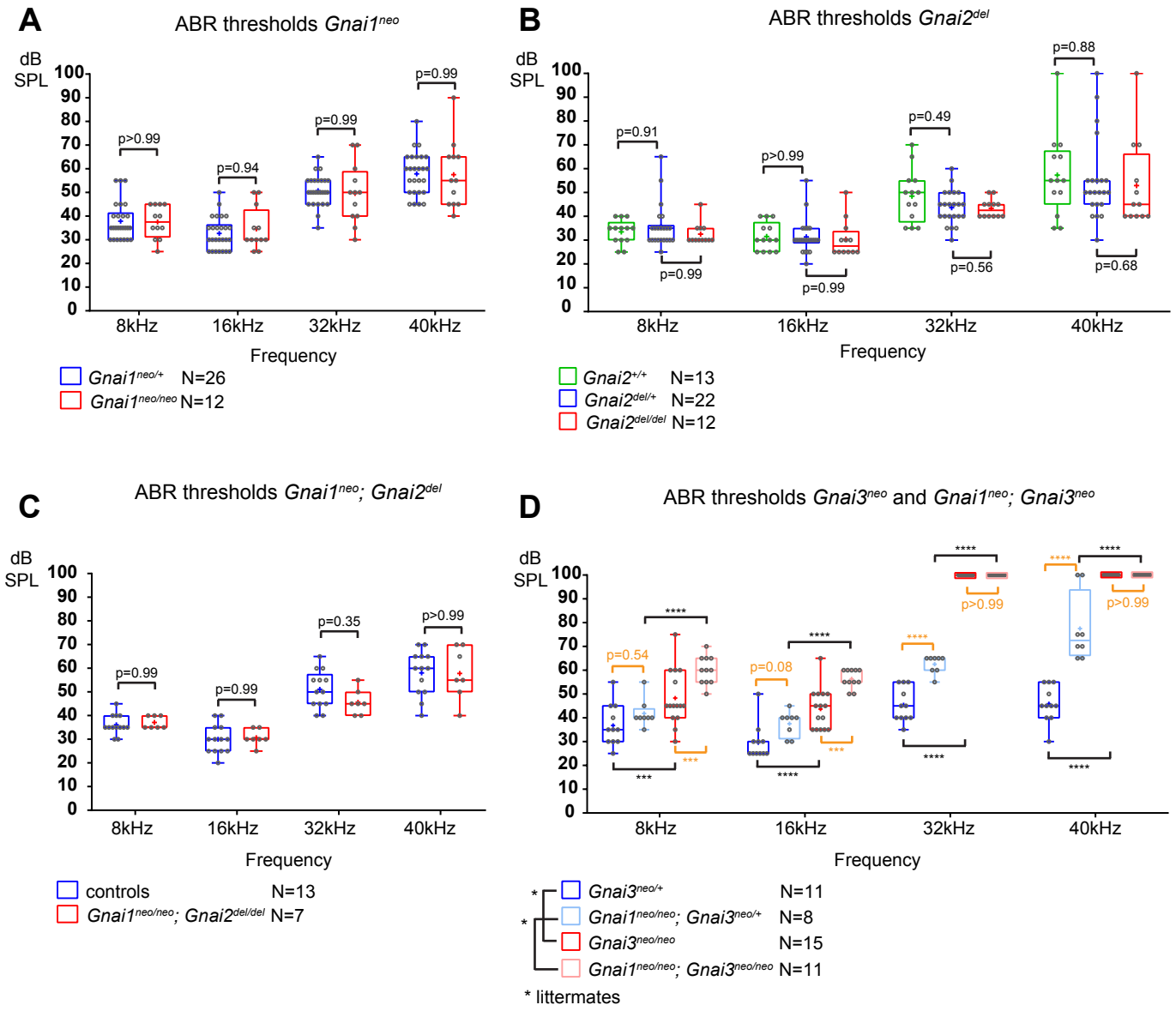

Figure 3. Loss of GNAI3 leads to profound deafness at high frequencies. A-D) ABR thresholds at 8, 16, 32, and 40 kHz for *Gnai1*^{neo} (A), *Gnai2*^{del} (B), *Gnai1*^{neo}*; Gnai2*^{del} (C), and *Gnai3*^{neo} and *Gnai1*^{neo}*; Gnai3*^{neo} (D) mutants tested between P21 and P29. Boxplots are framed with 25-75% whisker boxes where exterior lines show the minimum and maximum values, the middle line represents the median, and + represent the mean. A plotted value of 100 dB indicates that animals did not respond to 90 dB stimuli. In (C), controls are a pool of *Gnai1*$^{+/+}$*; Gnai2*$^{del/+}$, *Gnai1*$^{neo/+}$*; Gnai2*$^{+/+}$ and *Gnai1*$^{neo/+}$*; Gnai2*$^{del/+}$ animals. N indicates the number of animals tested. Two-way ANOVA with Sidak's multiple comparison. p<0.0001 ****, p<0.001 ***, p<0.01 **, p<0.05 *; non-significant p-values are indicated. P-values in orange were obtained comparing non-littermate animals and suggest possibly raised thresholds when GNAI1 is inactivated in addition to GNAI3 (see text). kHz, kilohertz, dB SPL, decibel sound pressure level.

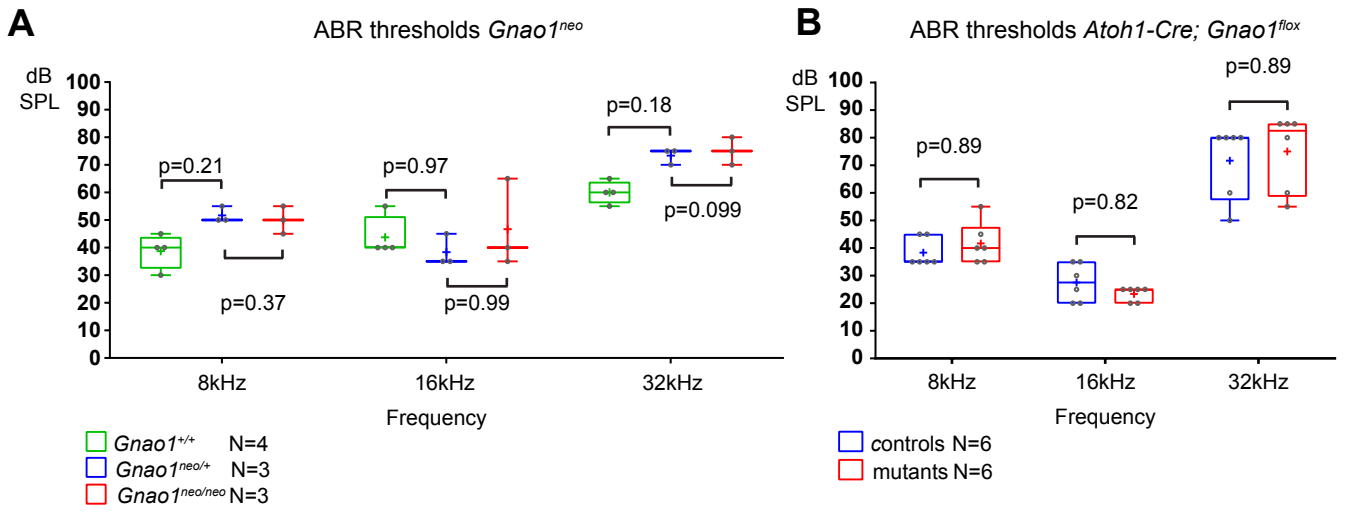

Figure 3 Supplement 1. A-B) ABR thresholds at 8, 16, 32 kHz for constitutive *Gnao1* (A) and conditional *Atoh1-Cre; Gnao1*$^{flox/flox}$ (B) mutants tested between P20 and P25. Boxplots are framed with 25-75% whisker boxes where exterior lines show the minimum and maximum values, the middle line represents the median, and + represent the mean. N indicates the number of animals tested. In (B), because the original animal cohort was established to test whether the loss of GNAO could enhance defects in *Gnai1; Gnai3* double mutants (see Fig. 2 Supp. 1E-F), controls include the following genotypes: *Atoh1-Cre; Gnao1*$^{flox/+}$, *Gnao1*$^{flox/flox}$, *Gnai1*$^{neo/+}$*; Gnai3*$^{neo/+}$, *Gnai1*$^{neo/+}$, *Atoh1-Cre; Gnao1*$^{flox/+}$*; Gnai1*$^{neo/neo}$*; Gnai3*$^{neo/+}$ and *Gnai1*$^{neo/neo}$*; Gnai3*$^{neo/+}$ where other alleles are wild-type. Mutants include the following: *Atoh1-Cre; Gnao1*$^{flox/flox}$; *Gnai3*$^{neo/+}$ and *Atoh1-Cre; Gnao1*$^{flox/flox}$*; Gnai1*$^{neo/neo}$*; Gnai3*$^{neo/+}$ where other alleles are wild-type. Cohort details can be found in the Source Data file. Two-way ANOVA with Sidak's multiple comparison. non-significant p-values are indicated. kHz, kilohertz, dB SPL, decibel sound pressure level.

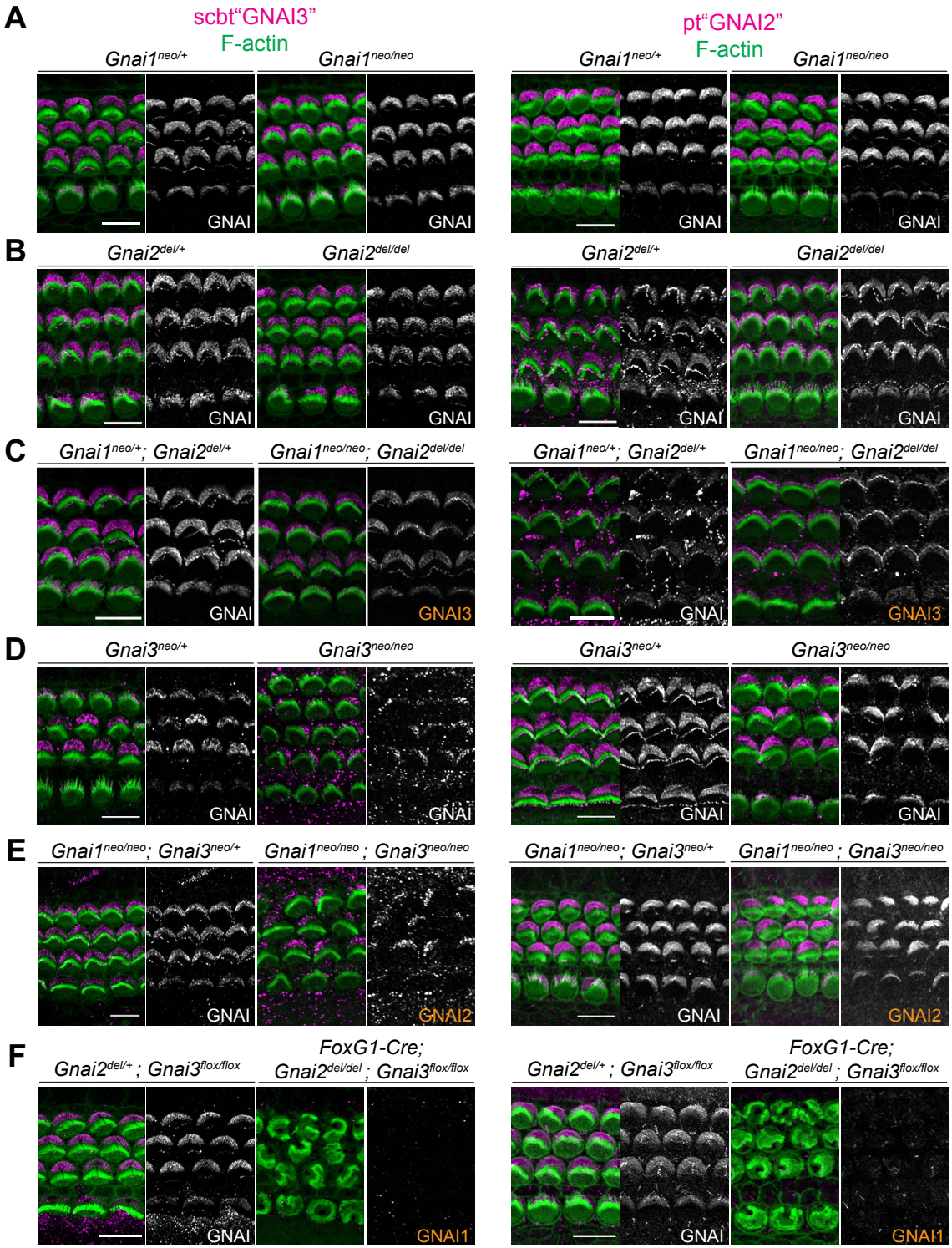

Figure 4. Systematic immunolabeling of GNAI proteins in *Gnai* mutant strains. A-F) Two different antibodies (scbt"GNAI3" and pt"GNAI2") were used to label the auditory epithelium at P0-P3. Neither antibody is specific for its protein target, as scbt"GNAI3" is able to detect GNAI2 (E) and pt"GNAI2" is able to detect GNAI3 (C). Note how no apical GNAI signal is visible with either antibody in *Gnai2; Gnai3* double mutants (F). When the identity of the GNAI protein detected is unambiguous based on the sample genotype, it is made explicit in orange. Scale bars are 10µm.

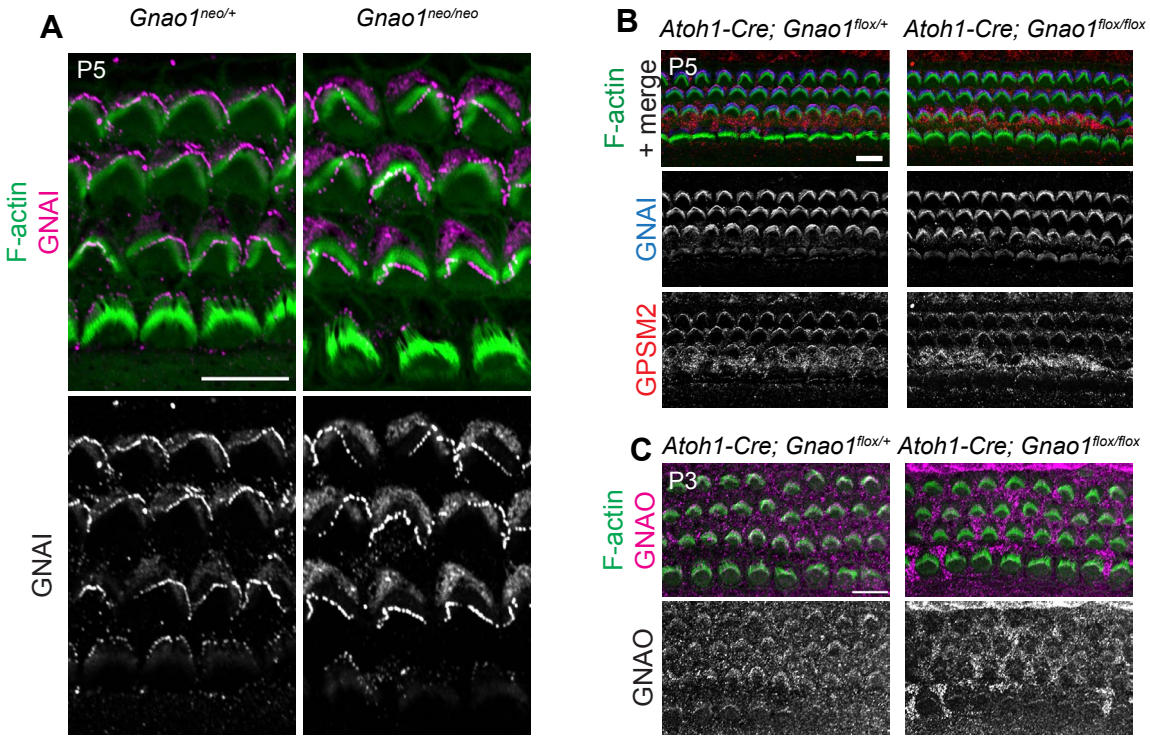

Figure 4 Supplement 1. GNAI protein distribution is undisturbed in *Gnao1* mutants and no evidence for specific GNAO enrichment at the hair cell apex. A-B) GNAI (scbt"GNAI3" antibody; see Fig. 4 and Methods) immunolabeling in P5 *Gnao1* constitutive (A) and *Atoh1-Cre; Gnao1*^{flox} conditional (B) mutants at the cochlear base. GNAI and GPSM2 (B) distribution at the bare zone and stereocilia tips is unchanged in absence of GNAO. **C)** GNAO immunolabeling at the P3 cochlear mid produces signals that are unspecific since they appear unchanged in conditional *Gnao1* mutants. Scale bars are 10μm.

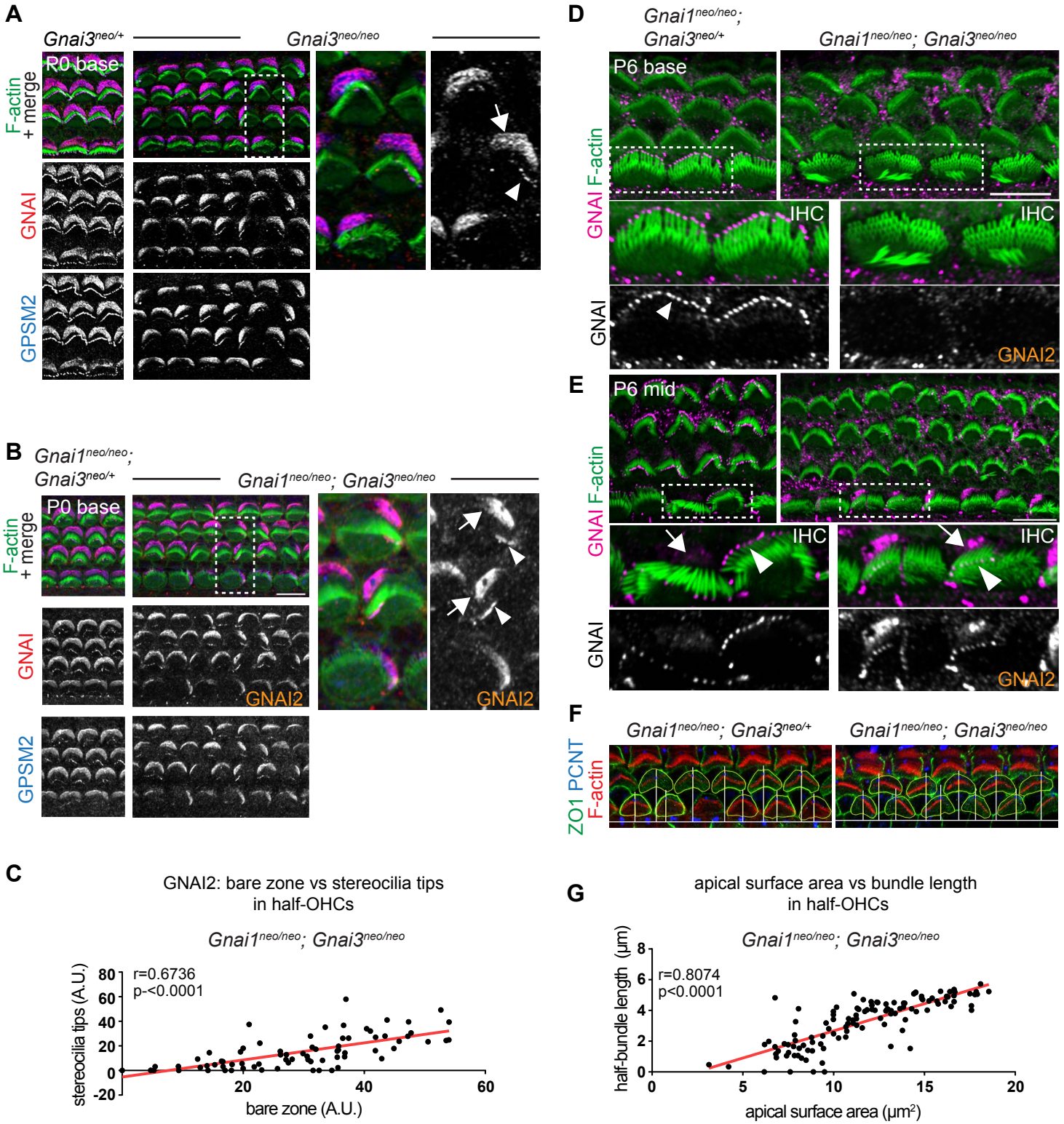

Figure 5. GNAI2 only partially rescues the loss of GNAI3 in individual postnatal hair cells. A-B) GNAI (pt"GNAI2" antibody; see Fig. 4) and GPSM2 co-immunolabeling in P0 *Gnai3*^{neo} (A) and *Gnai1*^{neo}*; Gnai3*^{neo} (B) animals at the cochlear base. Boxed regions are magnified on the right. In both mutants, incomplete GNAI patterns are observed at the bare zone (arrow) and stereocilia tips (arrowheads). Remaining GNAI signals are specifically GNAI2 in (B). **C)** Correlation plot of GNAI signal intensity at the bare zone and tips in half-OHCs at the P2 cochlear first turn. Presence or loss of GNAI is remarkably correlated spatially between bare zone and tips in the same half-HC. N=3 animals, n=37

OHCs, Pearson correlation with best fit (red line; plot for control littermates can be found in Fig. 5 Supp. 1A). **D-E)** GNAI (pt"GNAI2" antibody) immunolabeling in P6 *Gnai1*^{neo}*; Gnai3*^{neo} animals. Boxed IHC regions are magnified below. Loss of GNAI2 progresses with HC differentiation, with largely lost IHC signals at the P6 cochlear base (D) but partial rescue on one side of the cell at the P6 first turn (E), as observed at the cochlear base at P0 (A-B). **F-G)** ZO1 (apical junctions) and pericentrin (PCNT; basal body) immunolabeling in P8 OHCs. The position of the basal body was used to determine the vertex (middle) of the original hair bundle and to draw a radial line separating each OHC into two halves (F). The length of each hair bundle wing (y axis) is graphed in relation to the corresponding apical surface area (x axis) in the same half-OHC (G). Truncated OHC wings correlate with reduced apical membrane area on the same side. N=3 animals, n=58 OHCs, Pearson correlation with best fit (red line; plot for control littermates can be found in Fig. 5 Supp. 1C). A.U., arbitrary unit. Scale bars are 10µm.

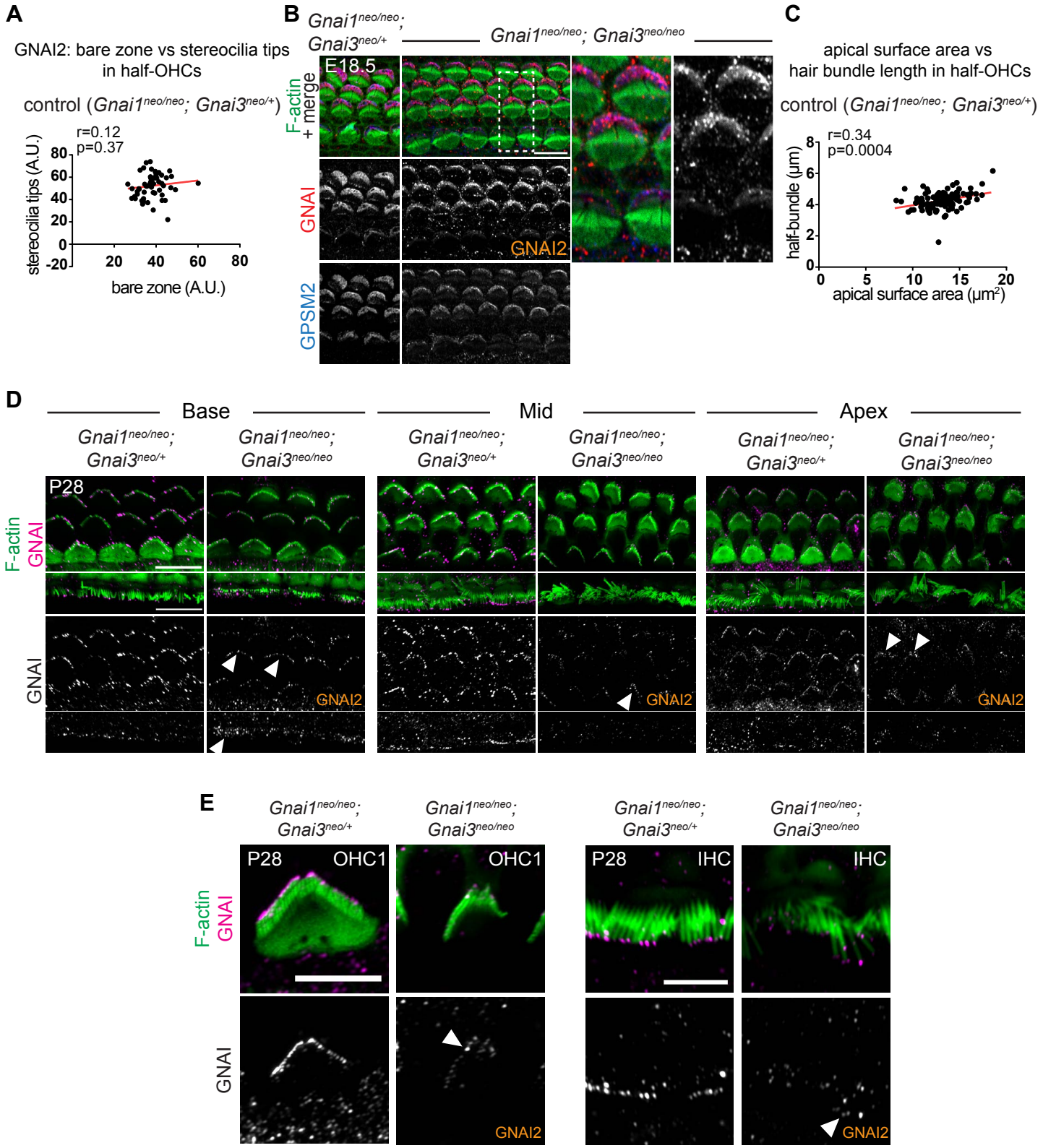

Figure 5 Supplement 1. GNAI2 fully rescues loss of GNAI3 at embryonic stages and is still detected in low amounts at stereocilia tips in adult hair cells lacking GNAI3. A) Control correlation plot for *Gnai1; Gnai3* double mutants in Fig. 5C. GNAI signal intensity at the bare zone and stereocilia tips in control half-HCs at the P2 cochlear base. N=3 animals, n=40 OHCs, Pearson correlation with best fit (red line). The graph shows relatively uniform GNAI enrichment in each sub-cellular compartment, unlike in *Gnai1; Gnai3* double mutants (Fig. 5C). **B)** GNAI (pt"GNAI2" antibody; see Fig. 4) and GPSM2

co-immunolabeling at the E18.5 5 cochlear base. As sole remaining GNAI, GNAI2 can still encompass the entire bare zone in *Gnai1; Gnai3* double mutants and no obvious hair bundle defects are observed, unlike at P0 (Fig. 5A-B). The boxed region is magnified to the right. **C)** Control correlation plot for *Gnai1; Gnai3* double mutants in Fig. 5G. The position of the basal body was used to determine the vertex (middle) of the hair bundle and to draw a radial line separating each OHC into two halves. The length of each hair bundle wing (y axis) is graphed in relation to the corresponding apical surface area (x axis) in the same half-OHC. The plot shows relatively uniform wing lengths and half apical areas in littermate controls, unlike in *Gnai1; Gnai3* double mutants (Fig. 5G). N=3 animals, n=52 OHCs, Pearson correlation with best fit (red line). **D-E)** GNAI (pt"GNAI2" antibody; see Fig. 4) immunolabeling in P28 adults. As sole remaining GNAI, GNAI2 can still be detected at low levels at stereocilia tips in *Gnai1; Gnai3* double mutants at the cochlear base, mid and apex (arrowheads). E) Higher magnifications views of a single OHC1 (left) and IHC (right). A.U., arbitrary unit. Scale bars are 10μm (B, D) and 5 μm (E).

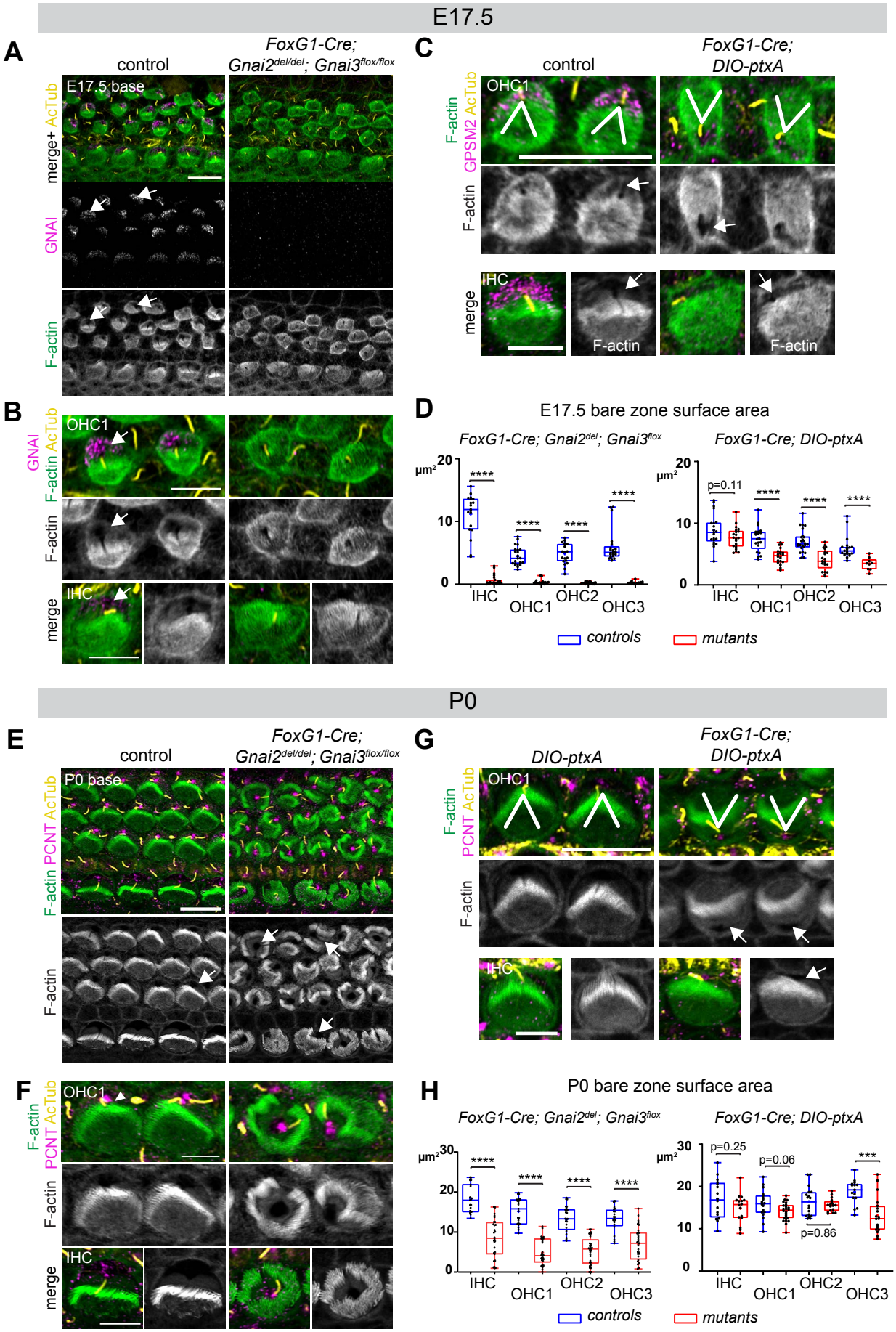

Figure 6. Delayed bare zone expansion and severely dysmorphic hair bundles in absence of

GNAI2 and GNAI3. A-B) GNAI (scbt"GNAI3" antibody, see Fig. 4) and acetylated tubulin (AcTub) co-immunolabeling at the E17.5 cochlear base. Note how F-actin labeling (phalloidin) reveals a polarized bare zone marked by GNAI (arrows) in control but not in *Gnai2; Gnai3* double mutants. **C)** GPSM2 and AcTub co-immunolabeling at the E17.5 cochlear base. In contrast to *Gnai2; Gnai3* double mutants, *FoxG1-Cre; DIO-ptxA* mutants have a polarized bare zone (arrows) despite OHC1-2 adopting a reversed orientation (V brackets indicate orientation). GPSM2 marks the bare zone in controls and is reduced in mutants. **D)** Graphs of bare zone surface area in E17.5 HCs at the cochlear base. *FoxG1-Cre; Gnai2*^{del}*; Gnai3*^{flox}: controls (*Gnai2*$^{del/+}$*; Gnai3*$^{flox/+}$ and *Gnai2*$^{del/+}$*; Gnai3*$^{flox/flox}$) N=3 animals, n=19 IHC, 23 OHC1, 19 OHC2, 21 OHC3; mutants N=3, n=23 IHC, 24 OHC1, 23 OHC2, 24 OHC3. *FoxG1-Cre; DIO-ptxA*: controls (*DIO-ptxA*) N=3, n=18 IHC, 18 OHC1, 21 OHC2, 18 OHC3; mutants N=3, n= 21 IHC, 20 OHC1, 21 OHC2, 9 OHC3. **E-G)** Pericentrin (PCNT) and AcTub co-immunolabeling at P0 at the cochlear base. Unlike at E17.5 (A-B, D), most P0 *Gnai2; Gnai3* double mutant HCs have a bare region (E-F, arrows). This bare region is unpolarized and its abnormal shape reflects aberrant stereocilia distribution. In sharp contrast, ptxA mutants have normally-shaped hair bundles and bare zones despite OHC1-2 adopting a reversed orientation (G). **H)** Graphs of bare zone surface area in P0 HCs at the cochlear base. *FoxG1-Cre; Gnai2*^{del}*; Gnai3*^{flox}: controls (*Gnai2*$^{del/+}$*; Gnai3*$^{flox/+}$, *Gnai2*$^{del/+}$*; Gnai3*$^{flox/flox}$ and *FoxG1-Cre; Gnai2*$^{del/+}$*; Gnai3*$^{flox/+}$) N=3, n= 19 IHC, 23 OHC1, 21 OHC2, 21 OHC3; mutant N=3, n= 21 IHC, 22 OHC1, 24 OHC2, 24 OHC3. *FoxG1-Cre; DIO-ptxA:* controls (*DIO-ptxA*) N=3, n=15 IHC, 23 OHC1, 18 OHC2, 15 OHC3; mutants N=3, n= 16 IHC, 24 OHC1, 18 OHC2, 19 OHC3. D, H: Mann-Whitney U test; $p<0.0001$ ****, $p<0.001$ ***, $p<0.01$ **, $p<0.05$ *; non-significant p-values are indicated. All *ptxA* samples are heterozygotes (*R26*$^{DIO\text{-}ptxA/+}$). Scale bars are 10μm (A, C (OHC), E, G (OHC)) and 5μm (B,C (IHC), F, G (IHC)).

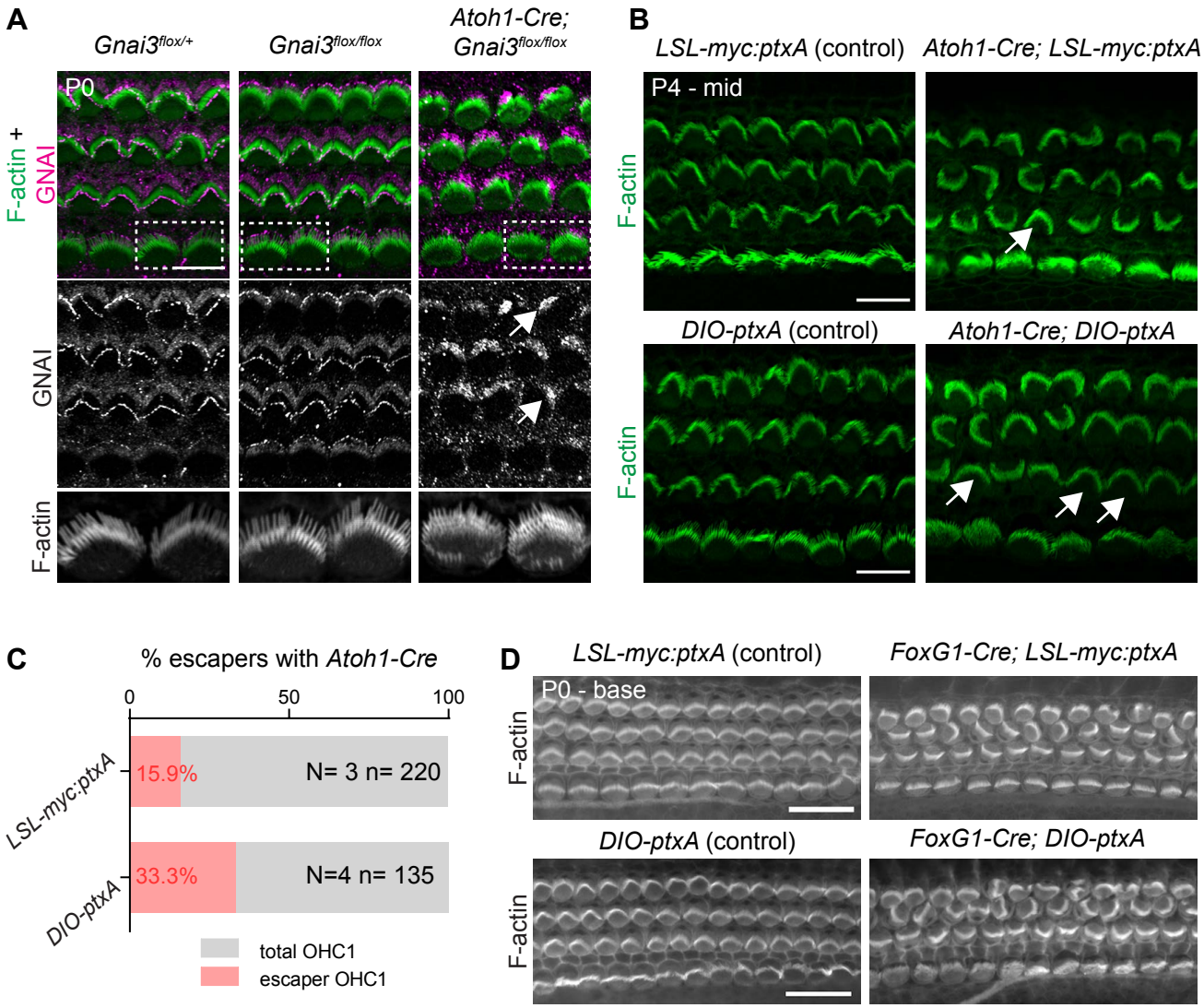

Figure 6 Supplement 1. Validation of the *Gnai3*^{flox} and *DIO-ptxA* mouse strains. A) GNAI (pt"GNAI2" antibody; see Fig. 4) immunolabeling at the P0 cochlear base. Note how in absence of Cre recombinase, *Gnai3*$^{flox/flox}$ HCs have normal hair bundles and normal GNAI enrichment at the bare zone and stereocilia tips. In contrast, breeding in *Atoh1-Cre* produces incomplete GNAI enrichment (arrows; compare with Fig. 4D) and shortened stereocilia typical of constitutive *Gnai3* mutants. Boxed IHC regions are magnified below. **B-D)** Comparison of the two *ptxA* strains used in this study (see also Fig. 2 Supp. 1C-D). B) PtxA expression with the *Atoh1-Cre* driver produces comparable P4 apical HC defects in the *LSL-myc:ptxA* and *DIO-ptxA* strains. "Escaper" OHC1 that are not inverted in orientation (arrows) likely do not express Cre, or did not undergo recombination. **C)** When *Atoh1-Cre* induces ptxA expression in post-mitotic HCs, the number of escaper OHC1 is higher in the *DIO-ptxA* strain. This is likely because *lox*-based genomic deletions (LSL) are favored over genomic inversions (DIO; see Fig. 2 Supp. 1C-D). **D)** In contrast, an earlier Cre driver (*FoxG1-Cre)* shows virtually no escapers in either strain. N and n indicate the number of animals and OHC1 analyzed, respectively. All *ptxA* samples in the study are heterozygotes (*R26*$^{LSL\text{-}myc:ptxA/+}$ or *R26*$^{DIO\text{-}ptxA/+}$). Scale bars are 10μm (A, B), 20μm (D).

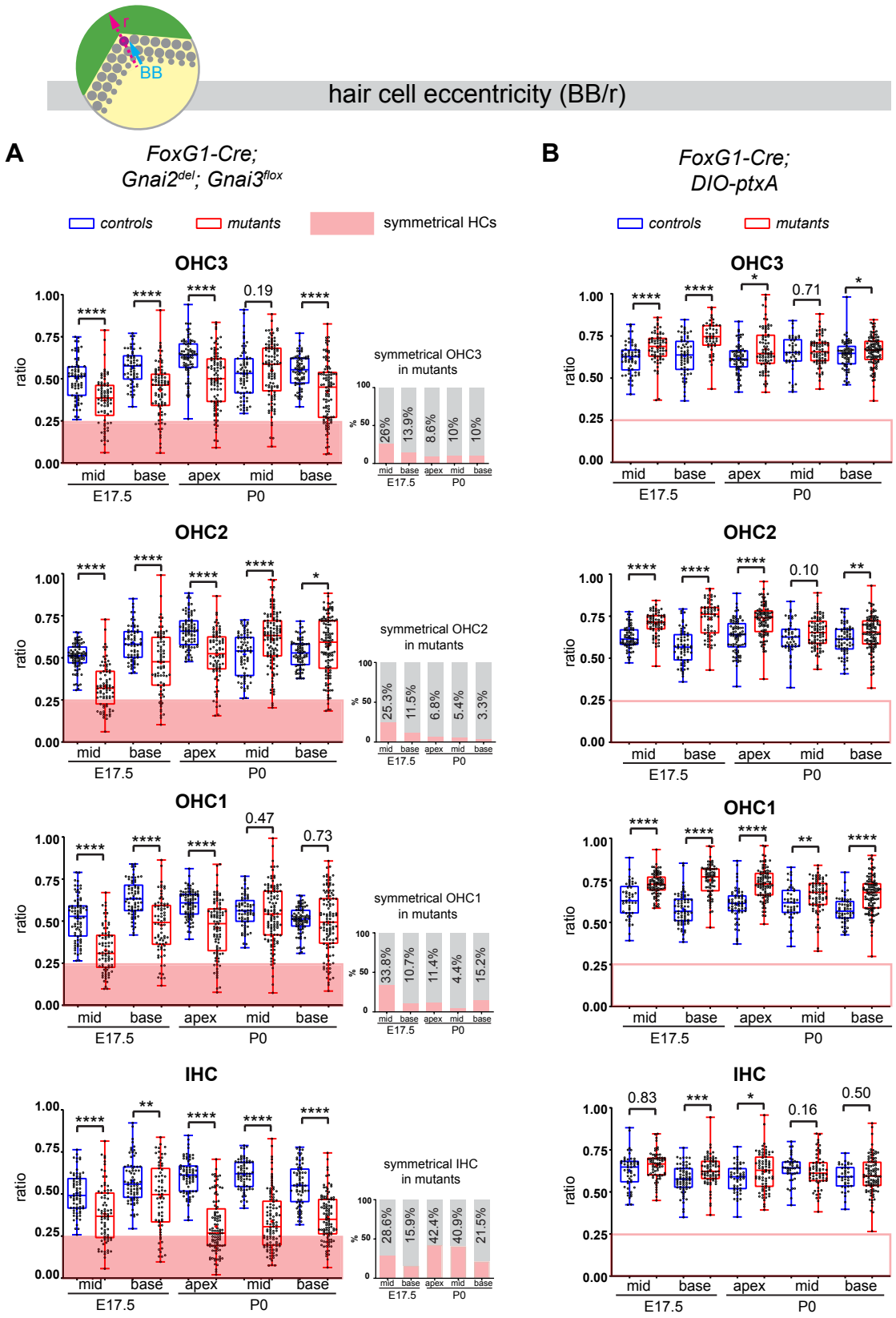

Figure 7. Loss of GNAI2 and GNAI3 provokes hair cell eccentricity defects absent in *ptxA* mutants. A-B) Graphs of HC eccentricity representing the position of the basal body as a ratio of the radius (BB/r, top diagram). Data cover E17.5 mid and base and P0 apex, mid and base cochlear positions for each HC type. HCs were considered symmetrical when their eccentricity ratio was lower than 0.25 (red zone). Only *FoxG1-Cre; Gnai2*^{del}*; Gnai3*^{flox} mutants harbor symmetrical HCs. Their

proportion is indicated in the bar graphs on the right (A). Overall, the proportion of symmetrical cells tends to decrease in maturing OHCs but remains higher in IHCs. At least 3 animals and 39 cells per HC type are represented for each stage, cochlear position and genotype (detailed in the Source Data file). Controls for *FoxG1-Cre; Gnai2*$^{del/del}$*; Gnai3*$^{flox/flox}$ are *Gnai2*$^{del/+}$*; Gnai3*$^{flox/+}$, *Gnai2*$^{del/+}$*; Gnai3*$^{flox/flox}$, *FoxG1-Cre; Gnai2*$^{del/+}$*; Gnai3*$^{flox/+}$ and *FoxG1-Cre; Gnai2*$^{del/+}$*; Gnai3*$^{flox/flox}$. Controls for *FoxG1-Cre; DIO-ptxA* are *DIO-ptxA* heterozygotes. Mann-Whitney U test: p<0.0001 ****, p<0.001 ***, p<0.01 **, p<0.05 *; non-significant p-values are indicated. Detailed cohort sizes and statistics can be found in Source Data file.OHCs but remains higher in IHCs. At least 3 animals and 39 cells per HC type are represented for each stage, cochlear position and genotype (detailed in the Source Data file). Controls for *FoxG1-Cre; Gnai2*$^{del/del}$*; Gnai3*$^{flox/flox}$ are *Gnai2*$^{del/+}$*; Gnai3*$^{flox/+}$, *Gnai2*$^{del/+}$*; Gnai3*$^{flox/flox}$, *FoxG1-Cre; Gnai2*$^{del/+}$*; Gnai3*$^{flox/+}$ and *FoxG1-Cre; Gnai2*$^{del/+}$*; Gnai3*$^{flox/flox}$. Controls for *FoxG1-Cre; DIO-ptxA* are *DIO-ptxA* heterozygotes. Mann-Whitney U test: p<0.0001 ****, p<0.001 ***, p<0.01 **, p<0.05 *; non-significant p-values are indicated. Detailed cohort sizes and statistics can be found in Source Data file.

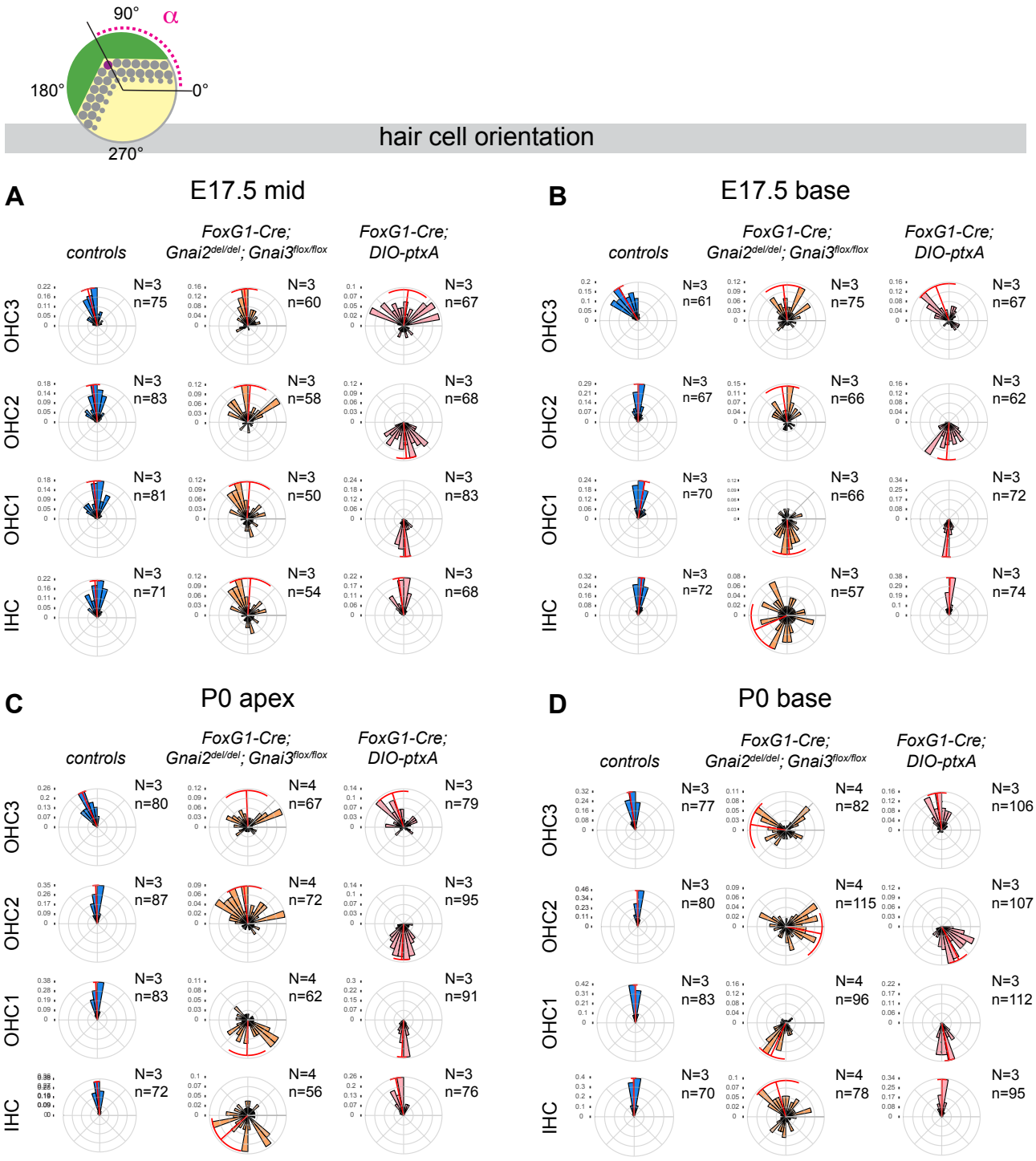

Figure 8. Loss of GNAI2 and GNAI3 recapitulates hair cell orientation defects observed in *ptxA* mutants. A-D) Circular histograms show HC orientation (α) based on the position of the basal body (purple dot in top diagram) at the stage and cochlear position indicated. 0° is towards the cochlear base and 90° is lateral. Only HCs with an eccentricity above 0.25 are represented (see Fig. 7). Histograms show frequency distribution (10° bins) and red radial lines and arcs respectively indicate the circular mean and the circular mean deviation. In control cochleae, HCs are tightly oriented laterally (90°) except for OHC3 that show a slight bias towards the cochlear apex (180°). As reported previously, ptxA expression induces a reversal of OHC1 and OHC2, and more imprecise lateral orientation of OHC3. This phenotype is progressively recapitulated in time in *Gnai2; Gnai3* double mutants (compare

least mature E17.5 mid (A) and most mature P0 base (D)). Interestingly, IHCs also show severe misorientation in *Gnai2; Gnai3* double mutants, unlike in *ptxA* mutants. n, HC number in N=3-4 animals. Controls for *FoxG1-Cre; Gnai2*$^{del/del}$*; Gnai3*$^{flox/flox}$ are *Gnai2*$^{del/+}$*; Gnai3*$^{flox/+}$, *Gnai2*$^{del/+}$*; Gnai3*$^{flox/flox}$, *FoxG1-Cre; Gnai2*$^{del/+}$*; Gnai3*$^{flox/+}$ and *FoxG1-Cre; Gnai2*$^{del/+}$*; Gnai3*$^{flox/flox}$. Histograms for littermate controls of *FoxG1-Cre; DIO-ptxA* mutants, as well as data at the P0 cochlear mid position, can be found in Fig. 8 Supp. 1. Detailed cohorts and results can be found in the Source Data file.

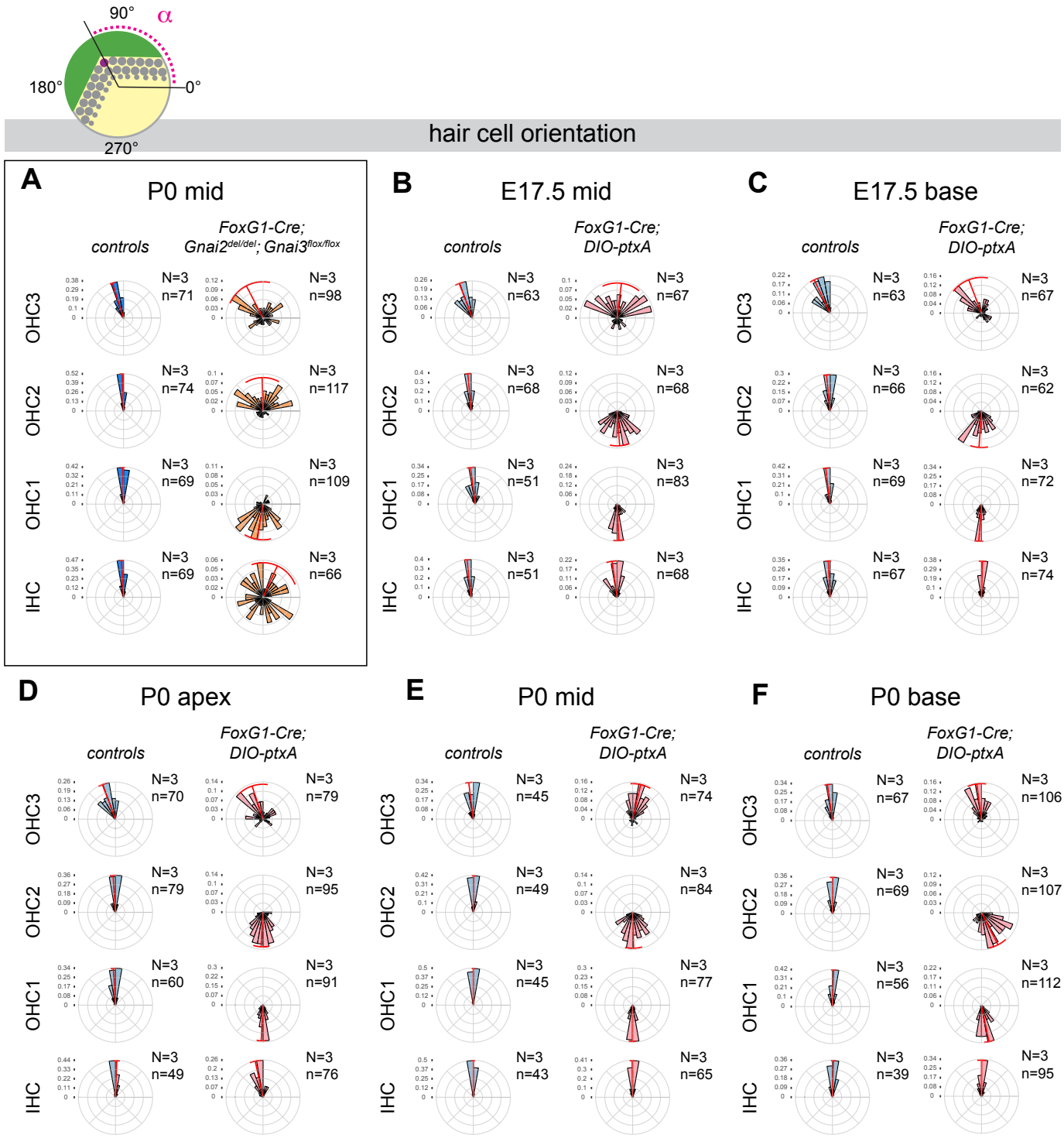

Figure 8 Supplement 1. Loss of GNAI2 and GNAI3 recapitulates hair cell orientation defects observed in *ptxA* mutants. A) P0 mid-cochlea histograms that complement P0 apex and P0 base histograms in Fig. 8C-D. **B-F)** Histograms including littermate controls for *FoxG1-Cre; DIO-ptxA* mutants in Fig. 8 (B-C, D, F), and P0 mid-cochlear position for *FoxG1-Cre; DIO-ptxA* mutants and controls (E). Note that all mutant histograms except at the P0 cochlear mid (A, E) are repeated from Fig. 8. Circular histograms show HC orientation (α) based on the position of the basal body (purple dot in top diagram) at the stage and cochlear position indicated. 0° is towards the cochlear base and 90° is lateral/abneural. Only HCs with an eccentricity above 0.25 are represented (see Fig. 7). Histograms show frequency

distribution (10° bins) and red radial lines and arcs respectively indicate the circular mean and the circular mean deviation. n, HC number in N=3-4 animals. Controls for *FoxG1-Cre; Gnai2*$^{del/del}$*; Gnai3*$^{flox/flox}$ are *Gnai2*$^{del/+}$*; Gnai3*$^{flox/+}$, *Gnai2*$^{del/+}$*; Gnai3*$^{flox/flox}$, *FoxG1-Cre; Gnai2*$^{del/+}$*; Gnai3*$^{flox/+}$ and *FoxG1-Cre; Gnai2*$^{del/+}$*; Gnai3*$^{flox/flox}$. Controls for *FoxG1-Cre; DIO-ptxA* are *DIO-ptxA* heterozygotes. Detailed cohorts and results can be found in the Source Data file.

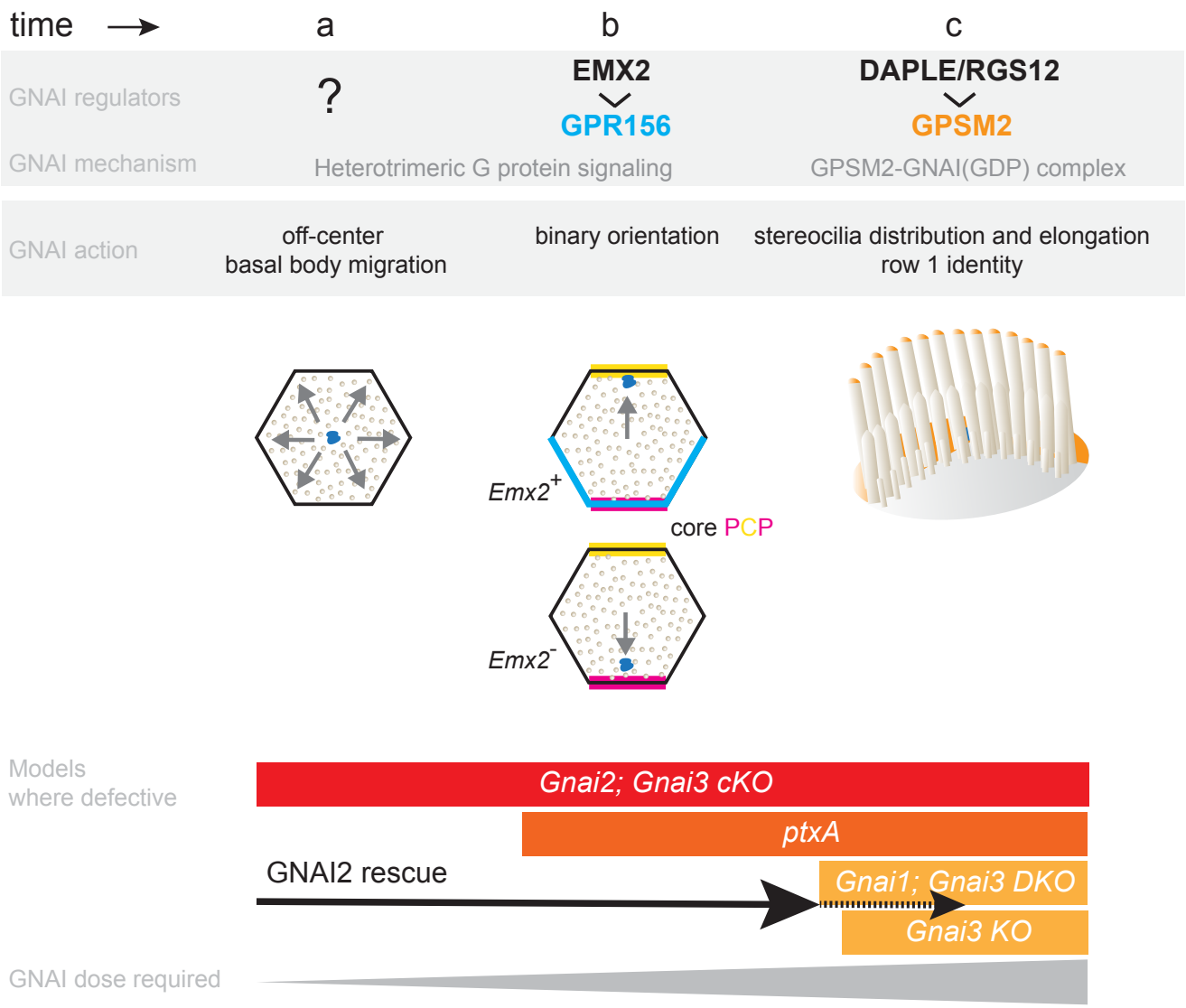

Figure 9. Summary and model: three roles validated in vivo for GNAI proteins during hair cell polarized morphogenesis. GNAI proteins are required for the centrifugal migration of the basal body, and thus HC symmetry breaking (a). This activity is distinct from defining binary HC orientation downstream of GPR156 (b), as *Gpr156* mutant HCs have normal basal body positioning and normal hair bundles. Finally, GNAI partners with GPSM2 to shape the hair bundle and elongate stereocilia (c). The specific identity and the dosage of the GNAI proteins required differ for each role. GNAI3 is the principal architect of hair bundle development (c), with GNAI2 playing an important but progressively waning role. In this role, high amounts of GNAI3/GNAI2 are required. A lower dose of any GNAI protein is sufficient for proper HC orientation (b), and a still lower dose can ensure symmetry breaking (a) since this function is intact in the *ptxA* model. We speculate that heterotrimeric signaling underpins basal body migration (a), as it does HC orientation (b). A regulator working with GNAI proteins for symmetry breaking remains to be identified.

Gene or model	Official name	Name in the study	MGI #	Reference	Allele description	Genetic background	Genetic background in the study	% surviving mutants at weaning age	
Gnai1	*Gnai1* ^{tm1Lbi}	*Gnai1* ^{neo}		Jiang et al, 2002 PMID: 36092739	neo cassette inserted in exon 3		129S1/SvImJ: C57BL/6J mix	*from het x het (expected 25%)* 16.4% (12 of 73 animals)	*from hom x het (expected 50%)* 45.8% (49 of 107 animals)
Gnai2	*Gnai2* ^{em1Btar}	*Gnai2* ^{del}		this study	CRISPR/Cas9 deletion of exons 2-3-4	C57BL/6J	C57BL/6J	9.9% (15 of 152 animals)	9.6% (5 of 52 animals)
							C57BL/6J: FVB/NJ mix	19.7% (12 of 61 animals)	46.7% (50 of 107 animals)
Gnai3	*Gnai3* ^{tm1Lbi}	*Gnai3* ^{neo}		Jiang et al, 2002 PMID: 36092739	part of intron 5 and exon 6 replaced with a neo cassette		129S1/SvImJ: C57BL/6J mix	30% (12 of 40 animals)	42% (63 of 150 animals)
		Gnai3 ^{flox}		this study	floxed exons 2-3	C57BL/6J	C57BL/6J		
Gnao1	*Gnao1* ^{tm1Lbi}	*Gnao1* ^{neo}	2152685	Jiang et al, 1998 PMID: 9501252	neo cassette inserted in exon 6	129S1/SvImJ	129S1/SvImJ	*from het x het (expected 25%)* 6.7% (3 animals out of 45)	
	Gnao1 $^{tm1c(EUCOMM)Hmgu}$	*Gnao1* ^{flox}	from 4456727	KOMP	floxed exon 3 - derived from Gnao1tm1a(EUCOMM)Hmgu via FLP-based removal of LacZneo cassette	C57BL/6N	C57BL/6N	*from Atoh1-Cre; het x het (expected 12.5% cKO)* 40% (10 *Atoh1-Cre; flox* hom of 25 animals)	*from Atoh1-Cre; hom x het (expected 25% cKO)* 30.7% (4 *Atoh1-Cre; flox* hom of 13 animals)
Gnai1; Gnai2	*Gnai1* ^{tm1Lbi} *; Gnai2* ^{em1Btar}	*Gnai1* ^{neo} *; Gnai2* ^{del}		Jiang et al, 2002 PMID: 36092739; this study			129S1/SvImJ: C57BL/6J:FVB/NJ mix	*from het; het x het; het (expected 6.25%)* 5,8% (7 of 121 animals)	*from hom; het x hom; het (expected 25% dKO)* 6.9% (2 of 29 animals)
Gnai1; Gnai3	*Gnai1* ^{tm1Lbi} *; Gnai3* ^{tm1Lbi}	*Gnai1* ^{neo} *; Gnai3* ^{neo}	5560183	Jiang et al, 2002 PMID: 36092739		129S1/SvImJ	129S1/SvImJ	*from hom; het x hom; het (expected 25% dKO)* 22.2% (20 of 90 animals)	*from hom; hom x hom; het (expected 50% dKO)* 43.2% (60 of 137 animals)
FoxG1-Cre; Gnai2; Gnai3		*Gnai2* ^{del} *; Gnai3* ^{flox}		this study			129S1/SvImJ: C57BL/6J:FVB/NJ mix	*second generation crosses* 0% (0 out of 149 animals)	*first generation crosses* 0.3% (1 out of 333 animals)
ptxA	*Gt(ROSA)26Sor* $^{tm1(ptxA)Cgh}$	*LSL-ptxA:myc*	3776029	Regard et al, 2007 PMID: 17992256	*loxP-stop-loxP* cassette before *ptxA:myc*	C57BL/6:129SvJ			
	Gt(ROSA)26Sor $^{em1(ptxA)Btar}$	*LSL-myc:ptxA*	6163665	Tarchini et al, 2016 PMID: 27660326	*loxP-stop-loxP* cassette before *myc:ptxA*	C57BL/6J	C57BL/6J		
		DIO-ptxA		this study	double inverted *lox* sites flanking *ptxA*	C57BL/6J	C57BL/6J		
Atoh1-Cre	*Tg(Atoh1-cre)1Bfri*	*Atoh1-Cre*	3775845	Matei et al, 2005 PMID: 16145671	randomly inserted transgene with *Atoh1* enhancer	(C57BL/6 x CBA)F1	C57BL/6		
FoxG1-Cre	*Foxg* $^{1tm1(cre)Skm}$	*FoxG1-Cre*	1932522	Hebert et al, 2000 PMID: 10837119	Cre knock-in in the *FoxG1* gene	129P2/OlaHsd-Hprtb-m3	129S1/SvImJ: C57BL/6J mix		

Supplementary Table 1. Mouse strain details.

Strain		Primer sequence	Bands size (bp)	
Gnao1 ^{flox}	forward	5' - TGGGTTTGATCCACAAGAGCGG - 3'		
	forward	5' - AGACGTGAAGCAGTACAAGC - 3'		
	reverse	5' - TCTCCTCAGTAGGGAAGATGGC - 3'		
			wt: 938; flox: 1119	wt: 387; flox: 421
Gnao1 ^{neo}	forward	5' - TGGTGACCCATTCTGACTTC - 3'		
	forward	5' - TCGCCTTCTATCGCCTTCTTGACG - 3'		
	reverse	5' - TTGGCAGAGAAAGCCCAAAG - 3'		
			wt: 836	neo: 461
Gnai1 ^{neo}	forward	5' - TCTAGGTGCTGGGGAATCTG - 3'		
	reverse	5' - GAGACGTGCTACTTCCATTTGTC - 3'		
	reverse	5' - TGAGCTTGTAGGCACAGAGG - 3'		
			wt: 1004	neo: 580
Gnai2 ^{del}	forward	5' -GCACCATCGTCAAGCAGATG - 3'		
	forward	5' - ATGGGTGGTTGTGAGCCATC - 3'		
	reverse	5' - GAGCTGGTATTCTCGTGAGC - 3'		
			wt: 728	wt: 1195; neo: 515
Gnai3 ^{neo}	forward	5' - CTTCTATCGCCTTCTTGACG - 3'		
	forward	5' -ACTCTGCTGACTTTGGCACC - 3'		
	reverse	5' - CTTTCATGCATTCGGTTCTG - 3'		
			wt: 762	neo: 450
Gnai3 ^{flox}	forward	5' - ATGAGGACGGCTATTCAGAG - 3'		
	reverse	5' - CATCCTACTTCACAAACTGC - 3'		XhoI digestion
			wt: 700; flox: 747	wt: 700; flox: 342 + 404
LSL-myc:ptxA	forward	5' - AAAGTCGCTCTGAGTTGTTAT - 3'		
	reverse	5' - GCGAAGAGTTTGTCCTCAACC - 3'		
	reverse	5' - GGAGCGGGAGAAATGGATATG - 3'		
			wt: 603	ptxA: 250
DIO-ptxA	forward	5' - GCACTTGCTCTCCCAAAGTC - 3'		
	reverse	5' - GGAGCGGGAGAAATGGATATG - 3'		
	reverse	5' - CGTCATTGACGTCAATAGGG - 3'		
			wt: 617	ptxA: 677
Atoh1-Cre	forward	5' - AGAGCGGCTGACAATAGAGG - 3'		
	reverse	5' - TTTCCATGAGTGAACGAACC - 3'		
			wt: no band	cre: 850
FoxG1-Cre	forward	5' - GCGACAAGAAGAACGGCAAG - 3'		
	forward	5' - GCAAGAACCTGATGGACATG - 3'		
	reverse	5' - AAGCACTTGTTGAGGGACAG - 3'		
	reverse	5' - TTTCCATGAGTGAACGAACC - 3'		
			wt: 202	cre: 381

Supplementary Table 2. Genotyping strategies.